Looking behind the scenes of Grubbs catalysis with the Unified Reaction Valley Approach

Marek Freindorf[a], Elfi Kraka[a,*]

[a]*CATCO Group, Chemistry Department, Southern Methodist University, Dallas TX*

ARTICLE INFO

Keywords:
Grubbs catalysis
URVA
DFT
IRC

ABSTRACT

In this study we analyzed the mechanism of [2+2] cycloaddition and cycloreversion reactions between trichlorovinylsilane and one first–generation Grubbs model catalyst **M1** with a $P(Me)_3$ ligand and two second– generation Grubbs model catalysts **M2** with an N–heterocyclic carbene (NHC) ligand and **M3** with a 2,5-di–methyl–NHC ligand. As a mechanistic tool we applied the Unified Reaction Valley Approach (URVA), based on reaction path calculations performed at the B3LYP/6–31G(d,p)/SDD(Ru) level of theory. In addition, for all stationary points of these reactions we performed a Local Mode Analysis (LMA) and QTAIM analysis of the electron density at the B3LYP/6–31G(d,p)/NESC/Jorge–TZP(Ru) and DLPNO–CCSD(T)/def2–TZVP/ECP(Ru) levels of theory. In all reactions investigated in this work four target bonds play a key role, either being formed and/or broken or changing from double to single bonds and vice versa during the catalytic process. As revealed by the URVA analysis in the cycloaddition reactions the bond forming events leading to the intermediate metallacyclobutane occur in a concerted fashion after the transition state (TS), i.e. this process does not contribute to the energy barrier. The bond breaking events of the following cycloreversion reactions transforming the intermediate into to final product are also concerted, however they occur before the TS, i.e. this process contributes to the barrier height. In this way URVA rationalizes why all cycloaddition reactions have a lower activation energies than their cycloreversion counterparts. According to our results, **M3** is the most effective model catalyst. Its activity is related to a strong stabilization of the metallacyclobutane intermediate and specific interactions between the reacting species and the methyl hydrogen atoms of the 2,5–di–methyl-NHC ligand of the catalyst . Based on LMA, we could also quantify the important role of a 4–center–2–electron α,β–(CCC) agostic interaction in the metallacyclobutane intermediate donating electron density to the Ru coordination center and facilitating the CC bond cleavage of the ring-opening cycloreversion step, lowering in this way the energy barrier. Overall, the new mechanistic details obtained with the URVA and LMA analysis can serve as a roadmap for the optimization of current and the future design of the next generations of Grubbs catalysts and beyond.

*Corresponding author
✉ ekraka@smu.edu (E. Kraka)
ORCID(s):

1. Introduction

Ru olefin metathesis complexes, known as first, second, and third–generation Grubbs catalysts and Hoveyda-Grubbs catalysts have become over the past decades one of the most prominent catalysts used for formation of new CC bonds [1–13]. A recent review of Jawiczuk at al. [14] gives a comprehensive summary of 30 years of Ru olefine metathesis and its use as a popular synthetic tool in academia and industry, ranging from pharmaceutical sciences [15–19] to petrochemical production [20–22]. The generally accepted mechanism of the olefin metathesis cycle [23] starts from a 16–electron alkylidene Ru(II) complex, which after dissociation of one ligand transforms into the active 14–electron form of the catalyst. The olefin binds to the active Ru-complex and undergoes a [2+2] cycloaddition reaction leading to an intermediate metallacyclobutane. The next step of the metathesis is the cycloreversion of the intermediate generating the new alkene and alkylidene. The pioneering work of Herisson and Chauvin [23] initiated numerous theoretical investigation over the past (see for example Ref.s [24–59, 14, 60]), which have contributed to our understanding of how structural and electronic features of a Ru-complex are coupled to its metathesis route, and have led to suggestion how to improve the turnover numbers of current catalysts in use. However, because of the complexity of the metathesis reaction, there are still numerous open questions.
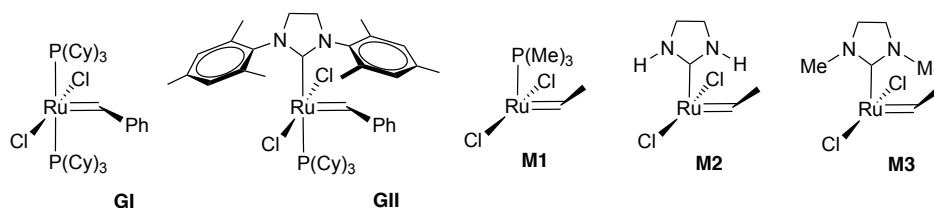

Figure 1: First and second–generation Grubbs catalysts **GI** and **GII** and the active form of three catalyst models (**M1**, **M2**, and **M3**) used in our study. Only selected hydrogen atoms are indicated.

The first–generation Grubbs catalyst (**GI**) dichloro(benzylidene)bis(tricyclohexylphosphine)ruthenium(II) has two tricyclohexylphosphine ($P(Cy)_3$) ligands coordinated to the central Ru(II) atom in *apical* position to the equatorial (($Cl)_2$Ru=CHPh) base (see Figure 1). The catalytic activity of **GI** was originally attributed to a strong σ donation from the $P(Cy)_3$ ligands to the metal center leading to the dissociation of one of the $P(Cy)_3$ ligands and resulting in the active 14–electron form of the catalyst [11, 1, 26]. In the second–generation catalyst (**GII**) dichloro[1,3-bis(2,4,6-trimethylphenyl)-2-imidazolidinylidene](benzylidene)(tricyclohexylphosphine)ruthenium(II) one of the $P(Cy)_3$ ligands is replaced with an N–heterocyclic carbene ligand (NHC), which is significantly bulkier than the trialkylphosphine (see Figure 1). Although NHC is a strong σ–electron donor, K–edge X–ray absorption spectroscopy has revealed that NHC ligation overall decreases electron density on the Ru center [61], which was supported by energy decomposition analyses [62, 60], showing that the interaction between NHC and the metal is due to both, σ–donation and π–back–donation effects. **GII** catalysts with an NHC ligand are generally showing higher catalytic activity than the **GI** bisphosphine complexes. They are more stable and inert while offering the possibility of steric and electronic modifications through substitutions of the NHC ligand [8, 9, 4, 2, 63, 64]. Modifications of NHC in complexes with different transition metals lead in the literature to formulation of descriptors analyzing the role of steric and electronic effects of this ligand [65], such as the buried volume [66], the extended Tolman electronic parameter [67–70], the ligand knowledge base [71, 72] and the molecular electrostatic potential [73]. The multivariate QSAR model derived from DFT calculations [74] provided a set of molecular descriptors for Grubbs catalysts, showing importance of the electronic effect described by a Wiberg bond index [75] and a σ bond order for the RuC bond, and the steric repulsion of the NHC ligand with alkylidene. Although, the improved catalytic activity of the second–generation catalysts seem to underly in the larger σ–donor and weaker π–acceptor properties of an NHC ligand compared to that of a phosphine ligand [62, 76], a more comprehensive explanation of the different catalytic activities of **GI** and **GII** catalysts, is still under dispute [77–80, 1, 26, 46, 49] and has to be further investigated.

Our work focused on exploring the mechanistic details of the [2+2] cycloaddition of the metathesis followed by the cycloreversion reaction, which according to pervious experimental observations [81] and DFT calculations [50] is the rate–determining steps of the entire metathesis cycle. We chose the reaction between trichlorovinylsilane and the

three Grubbs catalyst models **M1** - **M3** shown in Figure 1. Model **M1** mimics Grubbs catalyst **GI** and models **M2** and **M3** mimic Grubbs catalyst **GII**.
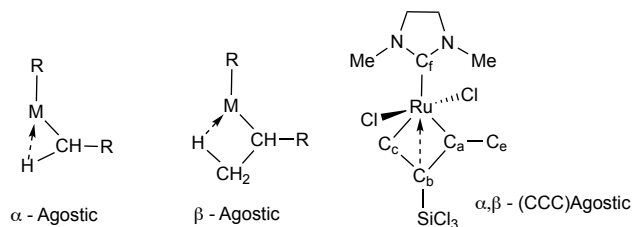

Figure 2: Different types of agostic bonding.

For both the first and second–generation Grubbs catalysts, the formation of a stable metallacyclobutane intermediate is a key element of the catalytic process, which is not fully understood yet. It has been suggested that the metallacyclobutane benefits from of a specific 4–center–2–electron interaction, coined α,β–(CCC) agostic bond with the metal [82, 83], which donates σ–electron density to the Ru center increasing the total electron density of the 16–electron Ru core [25, 28]. It has been further suggested that this interaction mimics α and β agostic hydrogen-bonding as sketched in Figure 2. Therefore, the investigation of the intermediate metallacyclobutane and the assessment of the proposed α,β–(CCC) agostic metal-bonding was one particular focus of our study.
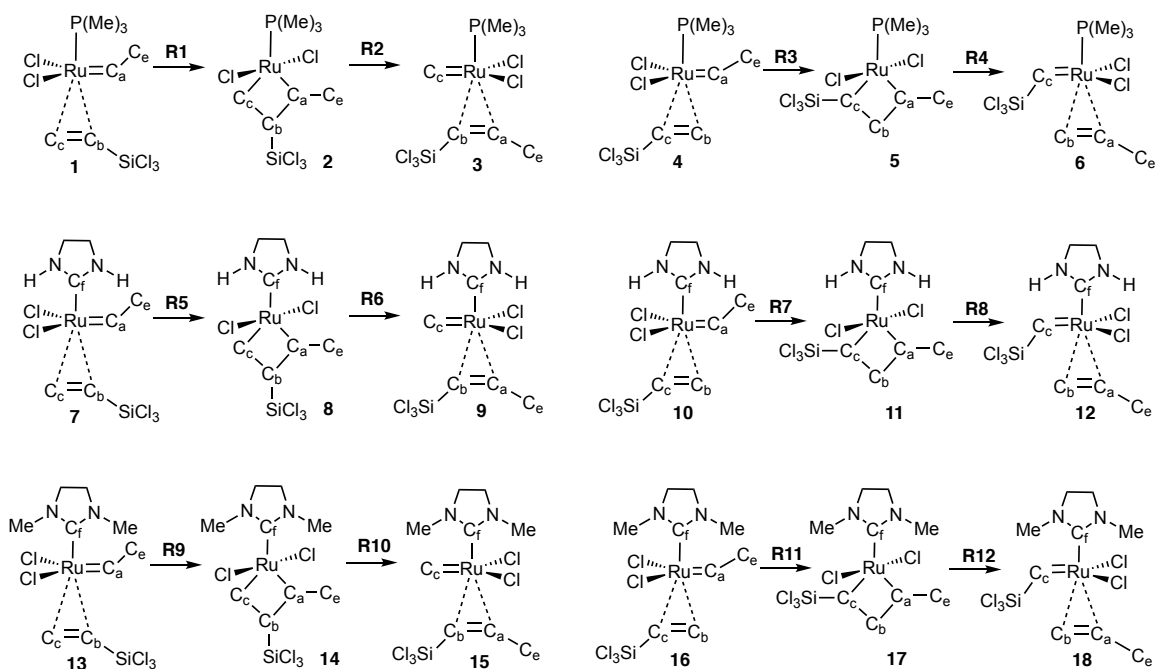

Figure 3: Molecular sketches of the reaction **R1** − **R12** investigated in our study. Only selected hydrogen atoms are indicated. For energetics see also Table 1.

Figure 3 summarizes all reactions investigated in this work. We investigated 6 different [2+2] cycloaddition and corresponding cycloreversion reactions resulting in a total of 12 reactions labelled as (**R1** – **R12**). The 6 metallacyclobutane intermediates are labelled as (**2**, **5**, **8**, **11**, **14**, and **17**). Reactions **R1** – **R4** describe the cycloaddition of trichlorovinylsilane to **GI** model **M1** accounting for the two different positions of the trichlorosilane substituent; reac-

tions **R5** – **R8** describe the cycloaddition of trichlorovinylsilane to **GII** model **M2** and reactions **R9** – **R12** describe the addition of trichlorovinylsilane to **GII** model **M3**, respectively.

2. Methodology

As a tool to shed more light into the details of the metathesis reactions we applied the *Unified Reaction Valley Approach* (URVA) [84], which provides comprehensive mechanistic information about a chemical reaction based on the curving of the reaction path [85–90] traced by the reaction compounds, i.e. the reaction complex on the potential energy surface (PES) from reactants, through transition state (TS) to products. Substantial changes in the reaction path curvature reflect important electronic and geometrical changes of the reaction complex, including bond cleavage, bond formation, charge polarization and transfer, rehybridization, etc. [84]. The scalar reaction curvature displayed as a function of the reaction coordinate provides a wealth of information. Curvature maxima indicate that substantial changes of the reaction complex are taking place, and curvature minima characterize a location on the reaction path were the reaction complex is preparing for a different chemical event [85, 88, 89, 91–95], allowing to divide the reaction into chemically meaningful reaction phases [86, 88]. The scalar reaction curvature is decomposed into internal components such as bond lengths, bond angles, dihedrals, etc. clarifying which internal parameters dominate a particular chemical event [85, 86]. If the contribution of a component has a positive sign, it supports the particular chemical event whereas a negative sign shows a resisting nature. URVA has provided new mechanistic insights into a variety of different chemical reactions, including the Diels-Alder reaction [96], cycloaddition to 1,3–dipoles [97, 98]; pseudopericyclic reactions [99], β–hydride elimination in Au complexes [100], Au assisted [3,3]–sigmatropic rearrangement [101], hydrogen release from water with borane and alane catalysts [102], the Claisen rearrangement of chorismate in the gas phase, water solution, and in *Chorismate Mutase* [103], and a hand-in-hand URVA and QTAIM Approach [104], just to name a few. Reaction path curvature profiles were complemented by the analysis of changes in the NBO charges [105–108] along the reaction path.

The URVA study was complemented by a comprehensive analysis of all stationary points; in particular the assessment of the bond strength of all target bonds via local vibrational mode force constants obtained from the *Local Mode Analysis* (LMA) [109]. The theoretical background of LMA, originally proposed by Konkoli and Cremer [110–114] can be found in Ref. [109]. LMAs have a number of special properties. Zou, Kraka, Cremer et al. verified the uniqueness of LMAs via an adiabatic connection scheme between local and normal vibrational modes [115]. In contrast to normal mode force constants, local mode force constants have the advantage of not being dependent of the choice of the coordinates used to describe the target molecule and in contrast to vibrational frequencies they are independent of the atomic masses. They are of high sensitivity to electronic structure differences (e.g., caused by changing a substituent) [109] and they directly reflect the intrinsic strength of a bond or weak chemical interaction as shown by Zou and Cremer [116]. LMA has been successfully applied to characterize covalent bonds [117–120, 116, 121–123] halogen bonds [124–128], chalcogen bonds [129–131], pnicogen bonds [132–134], and tetrel interactions [135] as well as H–bonding [136–142]. The LMA analysis was complemented with the analysis of the electron density using the quantum theory of atoms–in–molecule (QTAIM) [143, 144].

3. Computational Details

All 12 reactions of our study were analyzed with the following computational methods. As reaction path for each reaction we chose Fukui's intrinsic reaction coordinate path (IRC) [145] which was followed with the modified predictor-corrector method of Hratchian and Kraka[146] (step-size: 0.03 amu$^{1/2}$Bohr; tight geometry optimization convergence criterion) at the B3LYP/6–31G(d,p)/SDD(Ru) level of theory [147–150]. SDD is the abbreviation of the Stuttgart–Dresden effective core potential, which is a quasi-relativistic ab initio pseudopotential substituting the $M(Z-28)^+$–core orbitals of the second row transition elements, used together with the corresponding optimized GTO valence basis set and with the corresponding spin–orbit coupling operator [150]. All IRC calculations were performed with the Gaussian 16 package [151]. Geometries of all stationary points were reoptimized using the B3LYP/6–31G(d,p)/NESC/Jorge–TZP–DKH(Ru) level of theory [152]. The normalized elimination of the small component method NESC is an exact two–component relativistic method originally introduced by Dyall [153, 154]. In a series of previous publications [155–162], we report our NESC implementations with analytic gradients [163, 164] and analytic Hessians [165], which makes it possible to routinely carry out all–electron relativistic calculations for large

molecules with heavy atoms. These geometry optimizations were followed by single point energy point calculations at the DLPNO-CCSD(T)/def2–TZVP/ECP(Ru) [166, 167] level of theory with ORCA [168], using the optimal geometries from the B3LYP/6–31G(d,p)/NESC/Jorge–TZP–DKH(Ru) calculations. The URVA analysis of all reaction paths was performed with the COLOGNE package [169], and atomic charges were calculated using the NBO6 program [105].

Local vibrational modes and corresponding local mode force constants k^a at all stationary points were calculated using the LmodeA program [170]. Local mode force constants k^a of selected bonds can be transformed into bond strength orders (BSO) using a power relationship [89, 117]: $BSO = A * (k^a)^B$; where the constants A and B are determined by two reference molecules with known BSO and k^a values and the requirement that for a zero-force constant BSO becomes zero. For RuC bonds we chose as references the axial RuC bond of the CH_3 ligand in the $[(NHC)Cl_2(CH_3)Ru–CH_3]$ ruthenium complex and the RuC double bond in the $[(NHC)Cl_2Ru=CH_2]$ ruthenium complex. Based on the corresponding Mayer bond orders [171–173] of 1.072 and 1.870 and corresponding k^a values of 2.240 and 4.947 mDyn/Å calculated at the B3LYP/6–31G(d,p)/NESC/Jorge–TZP–DKH(Ru) level the power relationship constants for the RuC bonds are $A = 0.6085$ and $B = 0.7023$. For CC single and double bonds we chose C_2H_6 and C_2H_4 as references calculated at the the B3LYP/6–31G(d,p) level of theory. Based on BSO values of 1 and 2 and the corresponding k^a values of 4.157 and 9.899 mDyn/Å the power relationship constants for the CC bonds are $A = 0.3204$ and $B = 0.7989$. Bond strength orders BSO as a function of the local mode force constants k^a for reactions **R1** – **R12** are shown in Figures 10 – 12 of the Appendix.

Electron density $\rho(\mathbf{r})$ and energy density $H(\mathbf{r})$ were assessed with the AIMALL software package [174, 144, 143]. The covalent nature of the bonds was characterized following the Cremer-Kraka criterion, which implies that covalent bonding is characterized by a negative energy density, i.e., $H_b < 0$ at the bond critical point $\mathbf{r}_b$ between the two atoms forming the bond, whereas electrostatic interactions are indicated by positive energy density values, i.e., $H_b > 0$ [175–177]. The Laplacian of the electron density and the bond paths connecting bond critical points were evaluated with the AIMALL software package as well.

4. Results and Discussion

4.1. Energetics

Table 1 contains the energetics of reactions **R1** – **R12** investigated in our study at both the DFT and the CCSD(T) levels of theory. Reactant and product data are based on the IRC end-points, i.e. π–complexes of the Ru catalyst and the corresponding trichlorovinylsilane or metallacyclobutane intermediates (see Figure 3). The following discussion is based on the CCSD(T) free energies.

According to Table 1, the activation free energies G^a of the reactions **R1** – **R12** are in a range between of 2.4 and 17.1 kcal/mol, where the smallest G^a value of 2.4 kcal/mol is found for reaction **R9** and the largest value 17.1 kcal/mol is found for reaction **R10**, both belonging to the same metathesis cycle. The same trend is observed for all reactions investigated in our study showing that the first step, the [2+2] cycloaddition has a smaller activation free energy than the second step, the cycloreversion reaction. The decreasing G^a values of 8.5, 6.0, and 2.4 kcal/mol for the first step reactions **R1**, **R5**, and **R9** respectively, display the efficiencies of the different Grubbs catalysts. **M3**, the **GII** model with increased steric interactions shows best the performance. In comparison, the activation free energies G^a of the corresponding cycloreversion steps **R2**, **R6**, and **R10** are higher with values of 11.7, 12.8, and 17.1 kcal/mol, respectively. Furthermore, whereas for the [2+2] cycloaddition the barriers decrease from **M1** to **M3** for the cycloreversion step the barrier decrease from **M3** to **M1**. Similar trends hold for the [2+2] cycloaddition reactions **R2**, **R6**, and **R11**, which activation free energies G^a of of 6.0, 4.3, and 5.6 kcal/mol respectively and their cylcoreversion counterparts **R4**, **R8**, and **R12** with G^a values of 9.4, 10.5, and 13.1 kcal/mol, respectively; i.e. for cycloaddition reactions with a lower barrier the price to pay is a higher barrier for the following cycloreversion step. In summary, we observe that second–generation Grubbs catalysts show larger catalytic effects than first–generation catalysts, which can be increased via steric hindrance.

The formation of the intermediate metallacyclobutane intermediates **2**, **8**, and **14** changes from being slightly endothermic to exothermic in the series **M1**, **M2**, and **M3**, as reflected by the corresponding reaction free energies G_R of 0.6, -1.3, and -12.2 kcal/mol for reactions **R1**, **R5**, and **R9** respectively. A similar trend is found for reactions **R3**, **R7**, and **R11** with reaction free energies G_R values of 2.6, 0.4, -6.7 kcal/mol, respectively; identifying metallacyclobutane **14** as the most stable intermediate. This is in agreement with previous calculations [24] and experiments showing that

Table 1
Energetics (kcal/mol) of reactions **R1** − **R12** investigated in our study. Minimum geometries are calculated at the B3LYP/6–31G(d,p)/NESC/Jorge–TZP–DKH(Ru) level of theory, followed by single energy point calculations at the DLPNO-CCSD(T)/def2–TZVP/ECP(Ru)//B3LYP/6–31G(d,p)/NESC/Jorge–TZP–DKH(Ru) level of theory.

Reaction	DFT						CCSD(T)					
	E^a	E_R	H^a	H_R	G^a	G_R	E^a	E_R	H^a	H_R	G^a	G_R
R1	8.9	1.2	8.7	2.6	13.6	8.6	3.8	-6.8	3.7	-5.4	8.5	0.6
R2	10.4	-1.8	8.7	-3.4	8.6	-10.5	13.5	8.2	11.9	6.6	11.7	-0.5
R3	5.5	1.7	5.2	2.6	6.8	3.8	4.7	0.5	4.3	1.4	6.0	2.6
R4	9.1	-2.4	7.9	-3.0	7.9	-4.2	10.6	0.1	9.4	-0.5	9.4	-1.7
R5	10.4	1.9	9.6	2.8	10.6	4.3	8.2	-3.6	7.4	-2.8	8.5	-1.3
R6	10.1	2.1	8.4	0.5	8.3	-6.4	14.6	13.0	12.8	11.5	12.8	4.5
R7	5.3	0.7	5.0	1.8	6.4	2.6	3.2	-1.5	2.9	-0.4	4.3	0.4
R8	10.2	0.4	8.8	-0.2	9.0	-1.8	11.7	3.3	10.3	2.7	10.5	1.1
R9	3.5	-6.7	2.8	-5.7	2.5	-6.0	3.3	-12.9	2.6	-11.9	2.4	-12.2
R10	13.8	8.3	12.0	7.1	13.1	7.3	17.7	11.9	15.9	10.7	17.1	10.9
R11	3.9	-5.4	3.2	-4.4	3.6	-4.8	5.9	-7.3	5.2	-6.3	5.6	-6.7
R12	12.3	8.2	10.9	7.4	10.7	6.5	14.7	10.1	13.3	9.3	13.1	8.3

a metallacyclobutane of type **14** leads to the thermodynamically most stable to the final product [50, 81]. As expected, the cycloreversion reactions starting from the metallacyclobutane intermediates show an opposite trend. Reactions **R2**, **R6**, and **R10** become more endothermic with reaction free energies G_R of -0.5, 4.5, and 10.9 kcal/mol, respectively as well as reactions **R4**, **R8**, and **R12** with reaction free energies G_R of -1.7, 1.1, and 8.3 kcal/mol, respectively. While the energetics provide information about the overall catalytic effects, more details are obtained by an analysis of structure and bonding of the stationary points, which is topic of the next section.

4.2. Stationary Points

As described in the computational details, all stationary points are based on the transition states (TS) and the end–points of the IRC calculations. Reactants of the [2+2] cycloaddition step as well as the products of the retro-cyclization reactions are (π or van der Waals complexes) between the active form of the Grubbs catalyst and the trichlorovinylsilane, the metallacyclobutanes are the products of [2+2] cycloaddition as well as the reactants of the retro-cyclization reactions. As depicted in Figure 3, there are four specific bonds involved in the metathesis; in the [2+2] cycloaddition step the RuC double bond (RuC_a) of the active catalyst and the CC bond (C_bC_c) of trichlorovinylsilane transform into a single bonds while a new RuC single bond (RuC_c) and a new CC single bond (C_aC_b) are formed, leading to the metallacyclobutane intermediate. In the following retro-cyclization step, the RuC_c and the C_aC_b single bonds of the intermediate transform into double bonds and the (RuC_a) and (RuC_b) bonds are broken. Therefore, the central focus in this section is the LMA analysis and the electron density analysis of these target bonds. Table 2 presents bond lengths, local mode parameters and the electron density parameters for these four target bonds at the stationary points for reactions **R1** and **R2** with the catalyst **M1**. Because the product of **R1** and the reactant of t **R2** are identical Table 2 reports only values for the TS and the product of reaction **R2**. The same applies for other reactions investigated in this study, i.e. Tables 3 - 7.

According to Table 2, the strength of the C_aC_b bond is increasing from reactant **1**, **TS(1,2)**, to product **3** as reflected by the corresponding BSO values of 0.01, 0.06, and 0.48, respectively. We also observe that the energy density H_b becomes more negative, indicating on an increasing covalent character of this bond (H_b values are 0.0122 and -0.1483 Hartree/Bohr^3, for TS and product, respectively; no C_aC_b bond critical point was found for the reactant). These changes correlate with the changes in the bond length, which decreases (r values of 3.9879, 2.1941, and 1.5960 Å, for reactant, TS, and product, respectively). Simultaneously, the new RuC_c bond is emerging as reflected by the BSO values (0.03, 0.72, and 1.18, respectively) and H_b values, which reflect a weak electrostatic interaction of 0.0002 Hartree/Bohr^3 in reactant **1** and increasingly covalent interactions in **TS(1,2)** and product **3** (-0.0409, and -0.0719 Hartree/Bohr^3, respectively). The distance between C_a and C_b becomes smaller (r values of 3.3223, 2.1135, and

Table 2
Bond length r, local mode force constant k^a, local mode frequency ω^a, bond strength order BSO, electron density ρ at the bond critical point, energy density H_ρ at the bond critical point, for reactions **R1** and **R2**. For bond labeling see Figure 3. B3LYP/6–31G(d,p)/NESC/Jorge–TZP–DKH(Ru) level of theory.

Reaction/ Stat. point	Bond	r Å	k^a mDyn/Å	ω^a cm^{-1}	BSO	ρ e/Bohr^3	H_ρ Hartree/Bohr^3
R1							
1	RuC$_a$	1.8006	4.534	846.60	1.76	0.2125	-0.1232
TS(1,2)	RuC$_a$	1.8617	4.158	810.77	1.66	0.1878	-0.0990
2	RuC$_a$	1.9826	2.217	591.97	1.06	0.1455	-0.0694
1	C$_a$C$_b$	3.9879	0.021	76.40	0.01	-	-
TS(1,2)	C$_a$C$_b$	2.1941	0.121	185.11	0.06	0.0659	-0.0122
2	C$_a$C$_b$	1.5960	1.664	686.11	0.48	0.2060	-0.1483
1	C$_b$C$_c$	1.3414	8.971	1593.05	1.85	0.3385	-0.3759
TS(1,2)	C$_b$C$_c$	1.4343	3.879	1047.55	0.95	0.2840	-0.2673
2	C$_b$C$_c$	1.5893	1.876	728.40	0.53	0.2075	-0.1508
1	RuC$_c$	3.3223	0.013	45.58	0.03	0.0128	0.0002
TS(1,2)	RuC$_c$	2.1135	1.279	449.72	0.72	0.1044	-0.0409
2	RuC$_c$	1.9629	2.562	636.44	1.18	0.1497	-0.0719
R2							
TS(2,3)	RuC$_a$	2.1466	1.002	398.07	0.61	0.0992	-0.0382
3	RuC$_a$	4.3823	0.017	52.58	0.03	-	-
TS(2,3)	C$_a$C$_b$	1.4288	4.561	1135.84	1.08	0.2888	-0.2742
3	C$_a$C$_b$	1.3443	8.974	1593.29	1.85	0.3379	-0.3745
TS(2,3)	C$_b$C$_c$	2.2560	0.208	242.35	0.09	0.0607	-0.0095
3	C$_b$C$_c$	4.5801	0.015	65.27	0.01	-	-
TS(2,3)	RuC$_c$	1.8360	4.515	844.87	1.75	0.1968	-0.1075
3	RuC$_c$	1.7989	4.904	880.46	1.86	0.2121	-0.1243

1.9629 Å, respectively). The numbers in Table 2 also reflect the transformation of the RuC$_a$ and C$_b$C$_c$ double bonds into single bonds of the metallacyclobutane intermediate **2**; BSO values of the RuC$_a$ bond change from 1.76, 1.66, to 1.06, H_b becomes less negative (-0.1232, -0.0990, and -0.0694 Hartree/Bohr^3, respectively) and the bond length increases r value of 1.8006, 1.8617, and 1.9826 Å, respectively). The BSO values of the bond C$_b$C$_c$ decrease from 1.85, 0.95, to 0.53, respectively, H_b becomes less negative (-0.3759, -0.2673, and -0.1508 Hartree/Bohr^3), and the CC bond length increases (r = 1.3414, 1.4343, and 1.5893 Å, respectively). It is interesting to notice that the BSO value of the C$_b$C$_c$ bond in **2** is smaller than 1.0, which indicates that this bond is weaker than the single CC bond in ethane, the same holds for the newly formed C$_a$C$_b$ bond. RuC$_a$ and RuC$_c$ bonds have BSO values close to reference value of 1.072 in the intermediate **2**, indicating their single bond character.

In reaction **R2** the RuC$_a$ and C$_b$C$_c$ bonds are cleaved and intermediate **2** transforms into the final product **3**. The strength of the bond RuC$_a$ is decreasing (BSO values are 1.06, 0.61, and 0.03, for **2**, **TS(2,3)** and **3** respectively), H_b becomes less negative (the H_b values are -0.0694 and -0.0382 Hartree/Bohr^3, respectively; no RuC$_a$ bond critical point was found for **3**). The RuC$_a$ bond length increases (r values of 1.9826, 2.1466, and 4.3823 Å, respectively). The strength of the bond C$_b$C$_c$ becomes smaller in this series (BSO values of 0.53, 0.09, and 0.01, respectively), H_b becomes less negative (-0.1508 and -0.0095 Hartree/Bohr^3, respectively, without a bond critical point for **3**), and the bond length r increases (r value of 1.5893, 2.2560, and 4.5801 Å, respectively). The C$_a$C$_b$ and RuC$_c$ bonds are changing their character from single double bonds. The strength of the C$_a$C$_b$ bond increases (BSO values of 0.48, 1.08, and 1.85, respectively), H_b becomes more negative (H_b values are -0.1483, -0.2742, and -0.3745 Hartree/Bohr^3, respectively), the bond length decreases (r value of 1.5960, 1.4288, and 1.3443 Å, respectively). Similarly, the strength of the RuC$_c$ bond increases (BSO values are 1.18, 1.75, and 1.86, respectively), H_ρ becomes more negative (H_b values of -0.0719, -0.1075, and -0.1243 Hartree/Bohr^3, respectively) and the corresponding bond length decreases (r value

of 1.9629, 1.8360, and 1.7989 Å, respectively).

Reactions **R3** and **R4** are similar to reactions **R1** and **R2**, however the ethylidine group and trichlorovinylsilane in reactions **R3** and **R4** are in an opposite orientation. In reaction **R3** the bond C_aC_b is formed, and according to Table 3 the strength of this bond is increasing in the same series (the BSO values of 0.15, 0.05, and 0.37, respectively), the energy density H_b becomes more negative (thevalues of -0.0185 and -0.1470 Hartree/Bohr^3, without a bond critical point for the reactant), and the bond length is decreasing (the r value of 2.9184, 2.1014, and 1.6295 Å, respectively). Similarly, the RuC_c bond in **R3** is formed, the strength of this bond is increasing (the BSO values of 0.45, 0.67, and 1.09, respectively), the energy density becomes more negative (the H_ρ values of -0.0191, -0.0394, and -0.0670 Hartree/Bohr^3, respectively), and the bond length is decreasing (the r value of 2.2952, 2.1154, and 1.9738 Å, respectively). The RuC_a bond is changing from a double to a single bond in the intermediate **5**, which is confirmed by the decreasing strength of this bond (the BSO values of 1.72, 1.57, and 1.09, respectively), the energy density becomes less negative (the H_ρ values of -0.1103, -0.0974, and -0.0746 Hartree/Bohr^3, respectively), and the bond length becomes larger (the r value of 1.8259, 1.8648, and 1.9575 Å, respectively). Similarly, the C_bC_c bond is changing its character from a double to a single bond. The strength of this bond becomes smaller (the BSO values of 1.36, 0.82, and 0.51, respectively), the energy density becomes less negative (the H_ρ values of -0.3181, -0.2658, and -0.1597 Hartree/Bohr^3, respectively), and the bond length becomes larger (the r value of 1.3857, 1.4345, and 1.5708 Å, respectively).

Table 3
Bond length r, local mode force constant k^a, local mode frequency ω^a, bond strength order BSO, electron density ρ at the bond critical point, energy density H_ρ at the bond critical point, for reactions **R3** and **R4**. For bond labeling see Figure 3. B3LYP/6–31G(d,p)/NESC/Jorge–TZP–DKH(Ru) level of theory.

Reaction/ Stat. point	Bond	r Å	k^a mDyn/Å	ω^a cm^{-1}	BSO	ρ e/Bohr^3	H_ρ Hartree/Bohr^3
R3							
4	RuC_a	1.8259	4.393	833.36	1.72	0.2008	-0.1103
TS(4,5)	RuC_a	1.8648	3.852	780.39	1.57	0.1857	-0.0974
5	RuC_a	1.9575	2.284	600.88	1.09	0.1517	-0.0746
4	C_aC_b	2.9184	0.377	326.58	0.15	-	-
TS(4,5)	C_aC_b	2.1014	0.092	161.21	0.05	0.0756	-0.0185
5	C_aC_b	1.6295	1.187	579.40	0.37	0.1923	-0.1317
4	C_bC_c	1.3857	6.086	1312.08	1.36	0.3114	-0.3181
TS(4,5)	C_bC_c	1.4345	3.242	957.59	0.82	0.2838	-0.2658
5	C_bC_c	1.5708	1.796	712.74	0.51	0.2149	-0.1597
4	RuC_c	2.2952	0.628	315.12	0.45	0.0712	-0.0191
TS(4,5)	RuC_c	2.1154	1.141	424.71	0.67	0.1035	-0.0394
5	RuC_c	1.9738	2.274	599.54	1.09	0.1432	-0.0670
R4							
TS(5,6)	RuC_a	2.1641	0.718	336.88	0.48	0.0954	-0.0355
6	RuC_a	2.5322	0.193	174.64	0.19	0.0462	-0.0066
TS(5,6)	C_aC_b	1.4220	4.005	1064.42	0.97	0.2960	-0.2869
6	C_aC_b	1.3591	7.769	1482.45	1.65	0.3326	-0.3602
TS(5,6)	C_bC_c	2.1830	0.148	204.69	0.07	0.0648	-0.0124
6	C_bC_c	3.1220	0.161	213.21	0.07	-	-
TS(5,6)	RuC_c	1.8421	4.092	804.29	1.64	0.1915	-0.1029
6	RuC_c	1.8315	4.291	823.62	1.69	0.1958	-0.1071

In reaction **R4** the RuC_a and C_bC_c bonds are cleaved, similar as in reaction **R2**. The strength of the RuC_a bond in reaction **R4** is decreasing (the BSO values of 1.09, 0.48, and 0.19, respectively), the energy density becomes less negative (the H_ρ values of -0.0746, -0.0355, and -0.0066 Hartree/Bohr^3, respectively), and the bond length is increasing (the r value of 1.9575, 2.1641, and 2.5322 Å, respectively). The strength of the breaking C_bC_c bond in **R4**, in decreasing (the BSO values of 0.51, 0.07, and 0.07, respectively), the energy density becomes less negative (the H_ρ values of -

0.1597 and -0.0124 Hartree/Bohr^3, respectively, without a bond critical point for the product), and the bond length is increasing (the r value of 1.5708, 2.1830, and 3.1220 Å, respectively). The C_aC_b bond becomes a double bond in the final product **6**. The strength of this bond is increasing (the BSO values of 0.37, 0.97, and 1.65, respectively), the energy density become more negative (the H_ρ values of -0.1317, -0.2869, and -0.3602 Hartree/Bohr^3, respectively), and the bond length is decreasing (the r value of 1.6295, 1.4220, and 1.3591 Å, respectively). Similarly, the RuC$_c$ bond is changing its character into a double bond, which is confirmed by the increasing strength (the BSO values of 1.09, 1.64, and 1.69, respectively), the decreasing energy density (the H_ρ values of -0.0670, -0.1029, and -0.1071 Hartree/Bohr^3, respectively), and the decreasing bond length (the r value of 1.9738, 1.8421, and 1.8315 Å, respectively). Overall, in reactions **R1** – **R4** with the **M1** catalyst, the change of the strength of the formed and cleaved bonds correlates with the change of the covalent character of these bonds, and the change of the bond lengths.
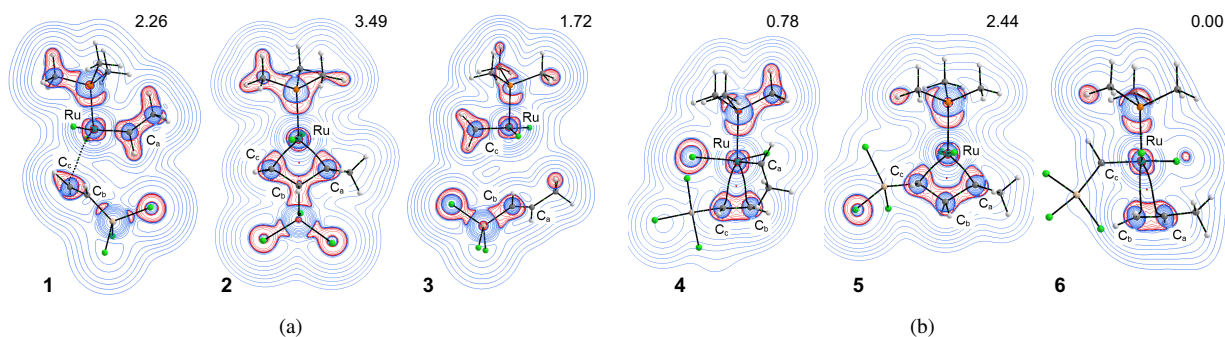

Figure 4: Contour map of the Laplacian of the electron density in the plane involving the Ru atom and selected two C atoms of the trichlorovinylsilane and ethylidene ligands; a) Molecules **1**, **2**, and **3** of reactions **R1** and **R2**; b) Molecules **4**, **5**, and **6** of reactions **R3** and **R4**. Blue lines correspond to positive Laplacian values (charge depletion), and red lines to negative Laplacian values (charge concentration). Relation paths and critical points involving Cl and H atoms are not shown for clarity. The numbers above the contours show the relative energy in kcal/mol. B3LYP/6–31G(d,p)/NESC/Jorge–TZP–DKH(Ru) level of theory.

Reactions **R1** and **R3** are similar. Both reactions form metallacyclobutane intermediates, i.e. **2** and **5** respectively. The only difference between these reactions is a relative position of the reactants. According to Table 1 the activation free energy of reaction **R1** is larger than the activation free energy of reaction **R3** (the G^a value of 8.5 and 6.0 kcal/mol, respectively). The larger activation free energy in **R1** can be related to a larger strength of all four bonds involved in formation of the intermediate **2** for the reactant and the TS. Therefore we have calculated the sum of the bond strengths for the all four bonds involved in the metallacyclobutane ring (RuC$_a$, C$_a$C$_b$, C$_b$C$_c$, and RuC$_c$) for the reactant and the TS of **R1**, and we found that the total bond strength of the forming cyclobutane ring in **R1** is larger than that in **R3** (sum of BSO values: 7.04 and 6.78, respectively). A similar correlation between the activation free energy and the total strengths of the four ring bonds is found for reactions **R2** and **R4**. The activation free energy of reaction **R2** is larger than in reaction **R4** (G^a value of 11.7 and 9.4 kcal/mol, respectively), and the total bond strength of the forming cyclobutane ring in **R2** is larger than in **R4** (sum of BSO values: 6.78 and 6.21, respectively).

Figure 4 shows contour maps of the Laplacian of the electron density in the plane defined by the Ru atom and two selected C atoms of the trichlorovinylsilane and ethylidene ligands for the reactants and products of reactions **R1** – **R4**. According to Figure 4 the most stable molecule in this series is the final product **6** of reaction **R4**, where the threechlorosilane group is located at the opposite side relative to the ethylidene group. There are two bond paths with two bond critical points for **6** between C$_a$ and Ru, and between C$_b$ and Ru. There is also in **6** a ring critical point involving these three atoms. The reactant **4** of the reaction **R3** is less stable than **6** (the relative DFT energy value of 0.78 kcal/mol) and there are also two bond paths with bond critical points between C$_b$ and Ru, and between C$_c$ and Ru, as well as a ring critical point involving these atoms. The intermediate **5** of reactions **R3** and **R4** is less stable than intermediate **2** (relative DFT energy value of 2.44 kcal/mol) but it has also two bond paths and bond critical points between C$_a$ and Ru, and between C$_c$ and Ru, as well as a ring critical point involving the Ru C$_a$, C$_b$, and C$_c$ atoms. Reactions **R1** and **R2** involve the threechlorosilane group at the same position relative to the ethylidene group, and according to Figure 4 the reactants and products are generally less stable than the corresponding reactants and products

Table 4
Bond length r, local mode force constant k^a, local mode frequency ω^a, bond strength order BSO, electron density ρ at the bond critical point, energy density H_ρ at the bond critical point, for reactions **R5** and **R6**. For bond labeling see Figure 3. B3LYP/6–31G(d,p)/NESC/Jorge–TZP–DKH(Ru) level of theory.

Reaction/ Stat. point	Bond	r	k^a	ω^a	BSO	ρ	H_ρ
		Å	mDyn/Å	cm^{-1}		e/Bohr^3	Hartree/Bohr^3
R5							
7	RuC$_a$	1.8217	4.538	847.00	1.76	0.2028	-0.1131
TS(7,8)	RuC$_a$	1.8604	4.112	806.28	1.64	0.1887	-0.0997
8	RuC$_a$	1.9808	2.282	600.61	1.09	0.1455	-0.0697
7	C$_a$C$_b$	3.0118	0.333	306.96	0.13	-	-
TS(7,8)	C$_a$C$_b$	2.2492	0.156	210.05	0.07	0.0616	-0.0097
8	C$_a$C$_b$	1.5986	1.673	687.93	0.48	0.2050	-0.1470
7	C$_b$C$_c$	1.3793	6.599	1366.24	1.45	0.3147	-0.3254
TS(7,8)	C$_b$C$_c$	1.4324	4.111	1078.33	0.99	0.2850	-0.2686
8	C$_b$C$_c$	1.5891	1.915	736.02	0.54	0.2080	-0.1512
7	RuC$_c$	2.3268	0.526	288.44	0.39	0.0670	-0.0178
TS(7,8)	RuC$_c$	2.1086	1.303	453.89	0.73	0.1061	-0.0423
8	RuC$_c$	1.9643	2.556	635.66	1.18	0.1493	-0.0721
R6							
TS(8,9)	RuC$_a$	2.1455	1.018	401.12	0.62	0.0998	-0.0388
9	RuC$_a$	4.2322	0.017	52.35	0.03	-	-
TS(8,9)	C$_a$C$_b$	1.4263	4.616	1142.67	1.09	0.2899	-0.2761
9	C$_a$C$_b$	1.3446	8.946	1590.76	1.84	0.3377	-0.3741
TS(8,9)	C$_b$C$_c$	2.2939	0.230	255.09	0.10	0.0580	-0.0083
9	C$_b$C$_c$	4.5585	0.015	65.16	0.01	-	-
TS(8,9)	RuC$_c$	1.8347	4.530	846.31	1.76	0.1977	-0.1084
9	RuC$_c$	1.7969	4.952	884.78	1.87	0.2136	-0.1261

of reactions **R3** and **R4**. We also observed that, except for intermediate **2**, reactants and products of reactions **R1** and **R2** do not have bond paths between the carbon atoms and Ru. However in **1**, there is a weak bond path between C$_c$ and Ru, which according to Table 2 also shows a bond critical point with a small positive energy density value (H_ρ value of 0.0002 Hartree/Bohr^3), indicating on a more electrostatic character of this interaction. Generally, according to Figure 4, the opposite orientation of the trichlorosilane group relative to the ethylidene group leads to more stable reactants and products in reactions **R3** and **R4**, which also according to Table 1 correlates with smaller activation free energies (tG^a values of 8.5 and 11.7 kcal/mol, for reactions **R1** and **R2**, and 6.0 and 9.4 kcal/mol, for reactions **R3**, and **R4**, respectively).

The next reaction paths involve reactions **R5** and **R6**, and the intermediate **8**, which are catalyzed by catalyst model **M2**. Table 4 presents the local mode and electron density parameters for the four target bonds in reactions **R5** and **R6**. The RuC$_a$ bond is monotonically changing its strength from a double bond in the reactant to a single bond in the product (BSO values of 1.76, 1.64, and 1.09, respectively), in line with changing its covalent character (H_ρ values of -0.1131, -0.0997, and -0.0697 Hartree/Bohr^3, respectively), and with increasing bond length (r value of 1.8217, 1.8604, and 1.9808 Å, respectively). The C$_a$C$_b$ bond is formed during this process, as reflected by the increasing BSO vales of 0.13, 0.07, and 0.48, respectively. Whereas there is no bond critical point for the reactant, there is a bond critical point for TS and product with an increasing covalent character (H_ρ values of -0.0097 and -0.1470 Hartree/Bohr^3, respectively), also reflected by a decreasing bond length (r value of 3.0118, 2.2492, and 1.5986 Å, respectively). The C$_b$C$_c$ bond, which has more double character in the reactant, is changing into a weak single bond in the product with less covalent character (BSO values of 1.45, 0.99, and 0.54; H_ρ values of -0.3254, 0.2686, and -0.1512 Hartree/Bohr^3, respectively), and increasing bond length (the r value of 1.3793, 1.4324, and 1.5891 Å, respectively). The RuC$_c$ bond is formed in this reaction with a monotonic change of bond strength (BSO values of 0.39, 0.73, and 1.18, respectively), covalent

character (H_ρ values of -0.0178, -0.0423, and -0.0721 Hartree/Bohr^3, respectively), and bond length (the r value of 2.3268, 2.1086, and 1.9643 Å, respectively).

Reaction **R6** starts from intermediate **8** and ends with the final product **9** breaking the RuC$_a$ and C$_b$C$_c$ bonds. The strength of the RuC$_a$ bond continuously decreases (BSO values of 1.09, 0.62, and 0.03, respectively), and its covalent character becomes smaller with no bond critical point found for the product (H_ρ values of -0.0697 and -0.0388 Hartree/Bohr^3, respectively), while its bond length is increasing (r value of 1.9808, 2.1455, and 4.2322 Å, respectively). The C$_a$C$_b$ bond transforms into a double bond in this reaction (BSO values of 0.48, 1.09, and 1.84, respectively) with increasing covalent character (H_ρ values of -0.1470, -0.2761, and -0.3741 Hartree/Bohr^3, respectively), and decreasing bond length (the r value of 1.5986, 1.4263, and 1.3446 Å, respectively). The C$_b$C$_c$ bond breaks (BSO values of 0.54, 0.10, and 0.01, respectively) decreasing its covalent character from the reactant to the TS (H_ρ values of -0.1512 and -0.0083 Hartree/Bohr^3, respectively), and increasing its bond length (r value of 1.5891, 2.2939, and 4.5585 Å, respectively). The RuC$_c$ double bond forms with increasing strength (BSO values of 1.18, 1.75, and 1.87, respectively), increasing covalent character (H_ρ values of -0.0721, -0.1084 and -0.1261 Hartree/Bohr^3, respectively), and decreasing bond length (r value of 1.9643, 1.8347, and 1.7969 Å, respectively).
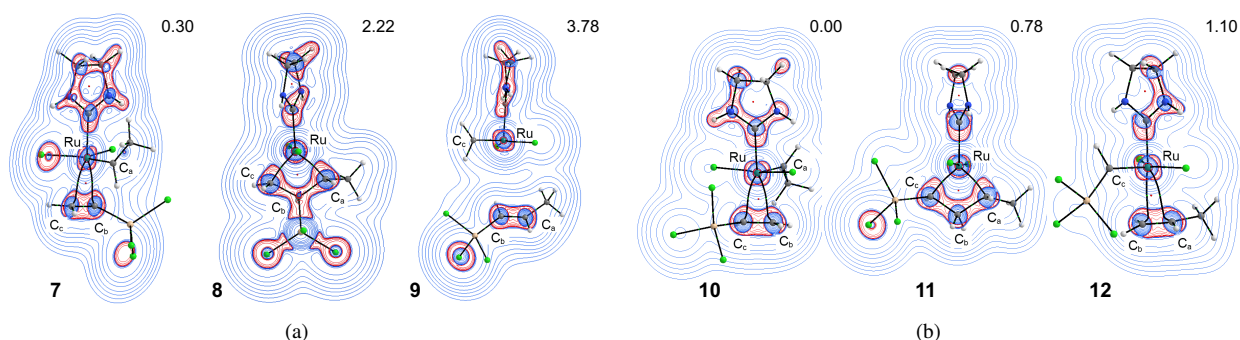

Figure 5: Contour maps of the Laplacian of the electron density in the plane defined by the Ru atom and two selected C atoms of the trichlorovinylsilane and ethylidene ligands; a) Molecules **7**, **8**, and **9** of the reactions **R5** and **R6**; b) Molecules **10**, **11**, and **12** of the reactions **R7** and **R8**. Blue lines correspond to positive Laplacian values (charge depletion), and red lines to negative Laplacian values (charge concentration). Relation paths and critical points involving Cl and H atoms are not shown for clarity. The numbers above the contours show the relative energy in kcal/mol. B3LYP/6–31G(d,p)/NESC/Jorge–TZP–DKH(Ru) level of theory.

The next path involves reactions **R7** and **R8**, which have an opposite orientation of the chlorovinylsilane reactant relative to the ethylidine group of the catalyst. Local mode and electron density parameters for these reactions are shown in Table 5. The trend of changes in bond strength, covalent character, and bond length in these reaction paths are quite similar as in the previous catalytic paths. In reaction **R7**, the RuC$_a$ bond is continuously decreasing its strength (BSO values of 1.71, 1.55, and 1.11, respectively), its covalent character (H_ρ values of -0.1097, -0.0980 and -0.0751 Hartree/Bohr^3, respectively), in parallel with increasing bond length (r value of 1.8261, 1.8641, and 1.9585 Å, respectively). The C$_a$C$_b$ bond becomes stronger and more covalent (BSO values of 0.13, 0.05, and 0.39 respectively; H_ρ values of -0.0177 and -0.1342 Hartree/Bohr^3, respectively; without a bond critical point for the reactant), and shorter (r value of 2.9544, 2.1141, and 1.6252 Å, respectively). The C$_b$C$_c$ bond becomes weaker (BSO values of 1.48, 0.87, and 0.52, respectively; H_ρ values of -0.3263, -0.2671, and -0.1583 Hartree/Bohr^3, respectively), and longer (r value of 1.3785, 1.4326, and 1.5737 Å, respectively). The RuC$_c$ bond becomes stronger (the BSO values of 0.44, 0.69, and 1.09, respectively; the H_ρ values of -0.0180, -0.0395, and -0.0672 Hartree/Bohr^3, respectively), and shorter (r value of 2.3262, 2.1198, and 1.9755 Å, respectively). In reaction **R8**, the strength of the RuC$_a$ bond is decreasing (BSO values of 1.11, 0.51, and 0.20, respectively; H_ρ values of -0.0751, -0.0361, and -0.0065 Hartree/Bohr^3, respectively), and the bond becomes longer (r value of 1.9585, 2.1624, and 2.5539 Å, respectively). At the same time, the strength of the C$_a$C$_b$ bond is increasing (BSO values of 0.39, 1.02, and 1.70, respectively; the H_ρ values of -0.1342, -0.2904, and -0.3635 Hartree/Bohr^3, respectively), with a decreasing bond length (r value of 1.6252, 1.4182, and 1.3562 Å,

Table 5
Bond length r, local mode force constant k^a, local mode frequency ω^a, bond strength order BSO, electron density ρ at the bond critical point, energy density H_ρ at the bond critical point, for reactions **R7** and **R8**. For bond labeling see Figure 3. B3LYP/6–31G(d,p)/NESC/Jorge–TZP–DKH(Ru) level of theory.

Reaction/ Stat. point	Bond	r Å	k^a mDyn/Å	ω^a cm^{-1}	BSO	ρ e/Bohr^3	H_ρ Hartree/Bohr^3
R7							
10	RuC$_a$	1.8261	4.347	829.00	1.71	0.2014	-0.1097
TS(10,11)	RuC$_a$	1.8641	3.781	773.17	1.55	0.1864	-0.0980
11	RuC$_a$	1.9585	2.348	609.25	1.11	0.1520	-0.0751
10	C$_a$C$_b$	2.9544	0.311	296.46	0.13	-	-
TS(10,11)	C$_a$C$_b$	2.1141	0.097	166.02	0.05	0.0745	-0.0177
11	C$_a$C$_b$	1.6252	1.289	603.84	0.39	0.1946	-0.1342
10	C$_b$C$_c$	1.3785	6.777	1384.61	1.48	0.0598	-0.3263
TS(10,11)	C$_b$C$_c$	1.4326	3.478	991.85	0.87	0.2847	-0.2671
11	C$_b$C$_c$	1.5737	1.842	721.87	0.52	0.2140	-0.1583
10	RuC$_c$	2.3262	0.636	317.04	0.44	0.0669	-0.0180
TS(10,11)	RuC$_c$	2.1198	1.187	433.14	0.69	0.1031	-0.0395
11	RuC$_c$	1.9755	2.308	604.06	1.09	0.1432	-0.0672
R8							
TS(11,12)	RuC$_a$	2.1624	0.780	351.19	0.51	0.0960	-0.0361
12	RuC$_a$	2.5539	0.207	180.71	0.20	0.0438	-0.0065
TS(11,12)	C$_a$C$_b$	1.4182	4.260	1097.80	1.02	0.2979	-0.2904
12	C$_a$C$_b$	1.3562	8.103	1514.02	1.70	0.3339	-0.3635
TS(11,12)	C$_b$C$_c$	2.2210	0.178	224.53	0.08	0.0616	-0.0105
12	C$_b$C$_c$	3.1760	0.151	206.67	0.07	-	-
TS(11,12)	RuC$_c$	1.8401	4.155	810.48	1.65	0.1927	-0.1041
12	RuC$_c$	1.8285	4.347	828.97	1.71	0.1973	-0.1087

respectively). The strength of the C$_b$C$_c$ bond is decreasing (BSO values of 0.52, 0.08, and 0.07, respectively; H_ρ values of -0.1583 and -0.0105 Hartree/Bohr^3, respectively; without a bond critical point for the product), and its bond length is increasing (r value of 1.5737, 2.2210, and 3.1760 Å, respectively). The strength of the RuC$_c$ bond is increasing (BSO values of 1.09, 1.65, and 1.71, respectively; H_ρ values of -0.0672, -0.1041, and -0.1087 Hartree/Bohr^3, respectively), and the bond becomes shorter (r value of 1.9755, 1.8401, and 1.8285 Å, respectively). Generally, the changes of the bond strength correlate well with the changes of the covalent character and the bond length for reactions **R5** – **R8**.

As for reactions **R1** – **R4**, we have calculated for he reactions **R5** – **R8** the total strength of the four target bonds in the reactant and the TS, which are involved in the formation and cleavage of the metallacyclobutane intermediates **8** and **11**. The bond strength of the four bonds forming the intermediate four-membered ring for reaction **R5** is larger than for reaction **R7** (sum of BSO values: 7.17 and 6.91, respectively), which correlates with the activation free energy of reactions **R5** and **R7** (G^a values of 8.5 and 4.3 kcal/mol, respectively). Similarly, the total bond strength of the four metallacyclobutane ring bonds in reaction **R6** is larger than that in reaction **R8** (sum of BSO values: 6.86 and 6.38, respectively), which also correlates with the activation free energies of reactions **R6** and **R8** (G^a values of 12.8 and 10.5 kcal/mol, respectively).

Figure 5 shows contour maps of the Laplacian of the electron density in the plane defined by the Ru atom and two selected C atoms of the reactants and products of the reactions **R5** – **R8**. According to Figure 5 the most stable molecule in this series is the initial reactant **10** of the reaction **R7**, which has two bond paths with two bond critical points between C$_b$ and Ru, and between C$_c$ and Ru, as well a ring critical point involving these three atoms. Similar as in the corresponding reactions **R3** and **R4** with the catalyst **M1**, the reactants and the products of the reactions **R7** and **R8** with opposite orientation of threechorosilane and ethylinyne groups, are more stable than the corresponding reactants and products of reactions **R5** and **R6** with the same group orientation. According to Figure 5 all reactants and products of reactions **R7** and **R8** show bond paths and bond critical points between Ru and carbon atoms, which

lead to their larger stabilization, and according to Table 1 to smaller activation barriers (G^a values of 8.5 and 12.8 kcal/mol, for reactions **R5** and **R6**, and 4.3 and 10.5 kcal/mol, for reactions **R7**, and **R8**, respectively)

Reactions **R9** – **R12** are catalyzed by **M3** where the hydrogen atoms of the NHC ligand are replaced by more bulky methyl groups (see Figure 3). We found similar changes of the bond strength, the covalent character and the bond length of the four target bonds RuC_a, C_aC_b, C_bC_c, and RuC_c, as for the reactions catalyzed by **M1** and **M2**, therefore below we will discuss in more details only changes of the RuC bond of the reactions catalyzed by **M3**.

Table 6
Bond length r, local mode force constant k^a, local mode frequency ω^a, bond strength order BSO, electron density ρ at the bond critical point, energy density H_ρ at the bond critical point, for reactions **R9** and **R10**. For bond labeling see Figure 3. B3LYP/6–31G(d,p)/NESC/Jorge–TZP–DKH(Ru) level of theory.

Reaction/ Stat. point	Bond	r Å	k^a mDyn/Å	ω^a cm^{-1}	BSO	ρ e/Bohr^3	H_ρ Hartree/Bohr^3
R9							
13	RuC_a	1.8345	4.262	820.83	1.68	0.1990	-0.1093
TS(13,14)	RuC_a	1.8501	4.178	812.69	1.66	0.1944	-0.1040
14	RuC_a	1.9876	2.256	597.27	1.08	0.1437	-0.0684
13	C_aC_b	2.8755	0.231	255.53	0.10	-	-
TS(13,14)	C_aC_b	2.4215	0.139	198.52	0.07	-	-
14	C_aC_b	1.5936	1.811	715.82	0.51	0.2076	-0.1500
13	C_bC_c	1.3731	6.829	1389.84	1.49	0.3187	-0.3337
TS(13,14)	C_bC_c	1.4077	4.159	1084.60	1.00	0.2995	-0.2954
14	C_bC_c	1.5878	2.011	754.30	0.56	0.2087	-0.1521
13	RuC_c	2.3376	0.408	253.93	0.32	0.0652	-0.0177
TS(13,14)	RuC_c	2.1719	0.633	316.42	0.44	0.0914	-0.0325
14	RuC_c	1.9660	2.609	642.25	1.19	0.1490	-0.0718
R10							
TS(14,15)	RuC_a	2.1770	0.851	366.88	0.54	0.0929	-0.0343
15	RuC_a	2.2235	0.924	382.14	0.58	0.0885	-0.0306
TS(14,15)	C_aC_b	1.4150	4.873	1174.12	1.14	0.2965	-0.2880
15	C_aC_b	1.4072	5.827	1283.82	1.31	0.3000	-0.2947
TS(14,15)	C_bC_c	2.3898	0.170	219.10	0.08	-	-
15	C_bC_c	3.0582	0.373	324.87	0.15	-	-
TS(14,15)	RuC_c	1.8282	4.570	850.02	1.77	0.2006	-0.1111
15	RuC_c	1.8000	5.045	893.04	1.90	0.2121	-0.1231

Local mode and electron density parameters for reactions **R9** and **R10** are shown in Table 6. According to Table 6, the strength of the RuC_a bond in reaction **R9** is decreasing (BSO values of 1.68, 1.66, and 1.08, respectively; H_ρ values of -0.1093, -0.1040, and -0.0684 Hartree/Bohr^3, respectively) and its length is increasing (r value of 1.8345, 1.8501, and 1.9876 Å, respectively). The strength of the RuC_c bond is increasing (BSO values of 0.32, 0.44, and 1.19, respectively; H_ρ values of -0.0177, -0.0325, and -0.0718 Hartree/Bohr^3, respectively), and the bond becomes shorter (r value of 2.3376, 2.1719, and 1.9660 Å, respectively). In reaction **R10** the RuC_a bond becomes weaker (BSO values of 1.08, 0.54, and 0.58, respectively; the H_ρ values of -0.0684, -0.0343, and -0.0306 Hartree/Bohr^3, respectively), and longer (the r value of 1.9876, 2.1770, and 2.2235 Å, respectively), while the RuC_c bond becomes stronger (BSO values of 1.19, 1.77, and 1.90, respectively; H_ρ values of -0.0718, -0.1111, and -0.1231 Hartree/Bohr^3, respectively) and shorter (r value of 1.9660, 1.8282, and 1.8000 Å, respectively).

Table 7 shows the local mode and electron density parameters for reactions **R11** and **R12**. The RuC_a bond in reaction **R11** becomes weaker (BSO values of 1.74, 1.68, and 1.13, respectively; H_ρ values of -0.1126, -0.1062, and -0.0742 Hartree/Bohr^3, respectively) and longer (r value of 1.8225, 1.8385, and 1.9630 Å, respectively), while the bond RuC_c in this reaction, becomes stronger (BSO values of 0.50, 0.44, and 1.11, respectively; H_ρ values of -0.0203, -0.0213, and -0.0660 Hartree/Bohr^3, respectively) and shorter (r value of 2.2812, 2.2719, and 1.9789 Å, respectively).

Table 7
Bond length r, local mode force constant k^a, local mode frequency ω^a, bond strength order BSO, electron density ρ at the bond critical point, energy density H_ρ at the bond critical point, for reactions **R11** and **R12**. For bond labeling see Figure 3. B3LYP/6–31G(d,p)/NESC/Jorge–TZP–DKH(Ru) level of theory.

Reaction/ Stat. point	Bond	r Å	k^a mDyn/Å	ω^a cm^{-1}	BSO	ρ e/Bohr^3	H_ρ Hartree/Bohr^3
R11							
16	RuC$_a$	1.8225	4.464	840.10	1.74	0.2029	-0.1126
TS(16,17)	RuC$_a$	1.8385	4.262	820.88	1.68	0.1975	-0.1062
17	RuC$_a$	1.9630	2.405	616.62	1.13	0.1508	-0.0742
16	C$_a$C$_b$	2.8394	0.495	374.39	0.18	-	-
TS(16,17)	C$_a$C$_b$	2.5342	0.298	290.19	0.12	-	-
17	C$_a$C$_b$	1.6148	1.484	647.91	0.44	0.1991	-0.1397
16	C$_b$C$_c$	1.3906	6.271	1331.85	1.39	0.3080	-0.3116
TS(16,17)	C$_b$C$_c$	1.3856	6.250	1329.64	1.39	0.3104	-0.3170
17	C$_b$C$_c$	1.5767	1.927	738.31	0.54	0.2131	-0.1571
16	RuC$_c$	2.2812	0.759	346.35	0.50	0.0734	-0.0203
TS(16,17)	RuC$_c$	2.2719	0.627	314.92	0.44	0.0747	-0.0213
17	RuC$_c$	1.9789	2.339	608.13	1.11	0.1420	-0.0660
R12							
TS(17,18)	RuC$_a$	2.2101	0.553	295.58	0.40	0.0865	-0.0298
18	RuC$_a$	2.4172	0.186	171.45	0.19	0.0571	-0.0120
TS(17,18)	C$_a$C$_b$	1.4029	4.545	1133.91	1.07	0.3070	-0.3075
18	C$_a$C$_b$	1.3654	6.786	1385.45	1.48	0.3278	-0.3502
TS(17,18)	C$_b$C$_c$	2.3368	0.124	187.08	0.06	0.0515	-0.0061
18	C$_b$C$_c$	2.9221	0.290	286.42	0.12	-	-
TS(17,18)	RuC$_c$	1.8312	4.168	811.71	1.66	0.1967	-0.1077
18	RuC$_c$	1.8223	4.289	823.46	1.69	0.1996	-0.1104

In reaction **R12**, the strength of the RuC$_a$ bond is decreasing (BSO values of 1.13, 0.40, and 0.19, respectively; H_ρ values of -0.0742, -0.0298, and -0.0120 Hartree/Bohr^3, respectively), and its length is increasing (r value of 1.9630, 2.2101, and 2.4172 Å, respectively), while the RuC$_c$ bond becomes stronger (BSO values of 1.11, 1.66, and 1.69, respectively; H_ρ values of -0.0660, -0.1077, and -0.1104 Hartree/Bohr^3, respectively), and shorter (r value of 1.9789, 1.8312, and 1.8223 Å, respectively).

As for the previous reactions, we have calculated the total strength of the four ring bonds for the reactant and the TS, in the reactions **R9** – **R12**, and correlated them with the corresponding activation free energies. The total bond strength of these bonds in reaction **R9** is smaller than that in reaction **R11** (sum of BSO values: 6.76 and 7.44, respectively), and the activation free energy in reaction **R9** is smaller than that in **R11** (G^a value of 2.4 and 5.6 kcal/mol). Similarly, the total strength of the ring bonds in reaction **R10** is larger than that in reaction **R12** (sum of BSO values: 6.87 and 6.41, respectively), which corresponds to a larger activation free energy in reaction **R10** compared with **R12** (G^a value of 17.1 and 13.1 kcal/mol).

Figure 6 shows the contour maps of the Laplacian of the electron density in the plane defined by the Ru atom and two selected C atoms of the reactants and products of reactions **R9** – **R12**. According to Figure 6 the most stable molecule in this series is intermediate **17**, which has two bond paths with two bond critical points between C$_a$ and Ru, and between C$_c$ and Ru, as well as a ring critical point involving Ru, C$_a$, C$_b$, and C$_c$ atoms. Similar as in the corresponding reactions with the catalysts **M1** and **M2**, the reactants and the products of reactions **R11** and **R12** with opposite orientation of threechorosilane and ethylinyne groups, are more stable than the corresponding reactants and products of reactions **R9** and **R10** with the same group orientation. According to Figure 6 all reactants and products of the reactions **R11** and **R12** show bond paths and bond critical points leading to larger stabilization, and according to Table 1 to generally smaller activation barriers (G^a values of 2.4 and 17.1 kcal/mol, for reactions **R5** and **R6**, and 5.6 and 13.1 kcal/mol, for reactions **R7**, and **R8**, respectively). It is interesting to note that contrary to reactions **R1** –
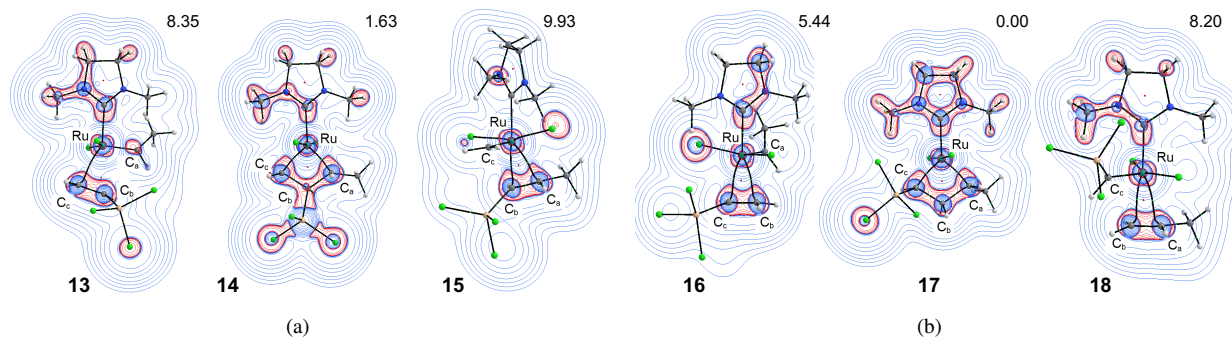
Figure 6: Contour maps of the Laplacian of the electron density in the plane defined by the Ru atom and two selected C atoms of the trichlorovinylsilane and ethylidene ligands; a) Molecules **13**, **14**, and **15** of the reactions **R9** and **R10**; b) Molecules **16**, **17**, and **18** of the reactions **R11** and **R12**. Blue lines correspond to positive Laplacian values (charge depletion), and red lines to negative Laplacian values (charge concentration). Relation paths and critical points involving Cl and H atoms are not shown for clarity. The numbers above the contours show the relative energy in kcal/mol. B3LYP/6–31G(d,p)/NESC/Jorge–TZP–DKH(Ru) level of theory.

R4 with catalyst **M1** and reactions **R5** – **R8** with catalyst **M2**, reactions **R9** – **R12** with catalyst **M3** show a stronger stabilization of the intermediate metallacyclobutanes **14** and **17**, relative to the corresponding reactants and products, which will be explained below.

4.3. Reaction Mechanism

The discussion of the reaction mechanisms in this section is based on the results from the URVA analysis, supported by NBO charge calculations along the reaction path. Because we are following the IRC in mass-weighted Cartesian coordinates reaction paths of different reactions can be overlaid leading to an effective one-to-one comparison [84], which is done in the following for energy profiles and changes of NBO charges along the reaction paths. Figure 7a shows an overlay of the energy profiles of reactions **R1** – **R4**, which are catalyzed by the phosphine model catalyst **M1**. The NBO charges along the reaction paths **R1** – **R4**, summed over all atoms of the catalyst (Cat) and all atoms of the ethylidene group and trichlorovinylsiliane groups (Mol), are shown in Figure 7b. The decomposition of the reaction curvature into selected internal components related to the target bonds RuC_a, C_aC_b, C_bC_c, and RuC_c in reactions **R1** – **R4**, are shown in Figures 7(c–f), which also include some additional internal components with a relatively large contribution to the reaction curvature. Generally, the reaction curvature shows maxima where bond forming or breaking processes takes place, and minima where the reaction complex relaxes and prepares for a different chemical event. The position of the minima are indicated in the plots by vertical lines with labels M1, M2, and so on, which divide the reaction path into reaction phases corresponding to different chemical events, with each reaction phase stretching from one minimum to the next embedding a curvature maximum. The gray bar in the plots indicates the chemical phase where bond formation or cleavage process takes place. The contributions of internal components to the reaction curvature are shown in the plots in different colors. A positive sign of a contribution indicates that this particular parameter supports the chemical change taking place whereas a negative sign is an indicator of a resisting effect.

Reaction **R1** starts from the reaction complex **1**, and makes the intermediate **2** forming the two C_aC_b and RuC_c bonds . According to Figure 7c, the largest supporting component to the curvature maximum in the chemical phase of this reaction is the C_aC_b bond length (blue line), indicating the formation of this bond. Similarly in the same phase, we observe a supporting contribution from the RuC_c bond length (red line), indicating the formation of this chemical bond. It is important to notice that both contributions to the curvature take place at the same value of the reaction parameter s, which indicates a concerted bond formation process. The C_aC_b contribution is larger than that of the RuC_c contribution, which indicates that the formation of the C_aC_b bond is connected with a larger electronic structure reorganization than the formation of the RuC_c bond, which is consistent our findings for other transition metals [84]. Reaction **R1** ends with the formation of intermediate **2**, which is characterized by a four–membered ring involving the RuC_b bond, which is responsible for an additional agostic interactions. According to Figure 7c, in the chemical phase of this reaction, there is also a supporting contribution to the curvature from the RuC_b bond (maroon
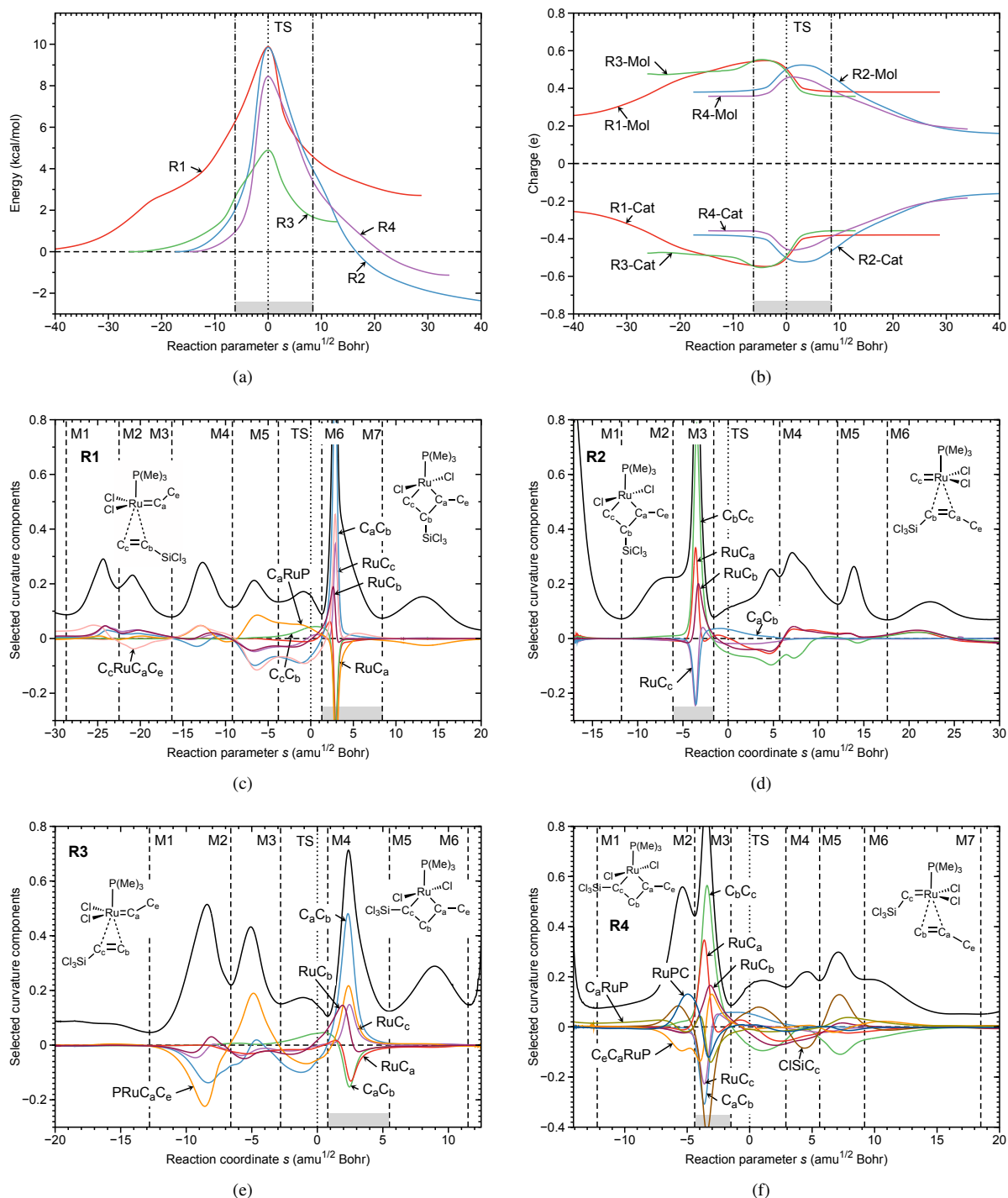
Figure 7: a) Energy profiles of reactions **R1 – R4**. b) Charge of the catalyst (Cat) and the reactants (Mol) of reactions **R1 – R4** . Decomposition of the curvature into internal components: c) for reaction **R1**; d) for reaction **R2**; e) for reaction **R3**; f) for reaction **R4**. Only selected hydrogen atoms are indicated. Curvature minima are shown as broken vertical lines and are labeled as M1, M2, and so on. Chemical phases where bonds are formed/cleaved, are indicated by a gray bar. The position of TS is indicated as a dotted line, and the vertical dash–dotted lines show the range of the chemical phases. B3LYP/6–31G(d,p)/SDD(Ru) level of theory.

line), which indicates that formation of the agostic bond takes place in a concerted way with with the formation of the C_aC_b and RuC_c bonds. In addition, we observe a resisting contribution from t the RuC_a bond, which according to Table 2 changes its character from a double to a single bond, i.e. it becomes weaker, and longer. There are also two additional internal components related to the C_aRuP (orange line) and $RuC_cC_aC_e$ angles (pink line), which are present in phase 5, 6, and 7. The C_aRuP component supports the reorganization of the reaction complex in a direction to the final product in phases 5 and 6, however resists this process in phase 7, where these two bonds are actually formed. The dihedral angle $RuC_cC_aC_e$ is related to the rotation of the ethylidine group around the RuC_a bond. It resists the reorganization of the reaction complex in the phases preceding the chemical phase, however it supports this process in the same phase where both chemical bonds are formed. It is interesting to notice that the chemical phase in which the most important chemical changes takes place occurs after the TS, where the reaction complex is already moving downhill on the potential energy surface. Therefore, the formation of the C_aC_b and RuC_c bonds does not contribute to the activation energy of this reaction and the energy needed to overcome the barrier is related to the geometry and electronic preparation of the reaction complex for the bond formation process. Therefore, modification of these preparatory process will influence the barrier height.

Reaction **R2** starts from intermediate **2** producing the final product **3** via cleavage of the two intermediate RuC_a and C_bC_c bonds. Thereaction path curvature and its decomposition is shown in Figure 7d. According to Figure 7d breaking of both bonds takes place in a concerted way in phase 3, as it is indicated by a supporting contribution of the RuC_a bond component (green line) and the C_bC_c bond component (red line) both adapting maxima in this phase. In the same phase we observe a resisting contribution from the RuC_c bond (violet line) and the C_aC_b bond (blue line), which are related to changing the bond character from a single to a double bond. Similarly as in reaction **R1** the supporting contribution of the C_bC_c component is larger than the RuC_a contribution, reflecting a larger reorganization of the reaction complex related to the cleavage of the C_bC_c bond. We also observe in the phase a supporting contribution from the RuC_b bond (maroon line) related to the cleavage of the agostic interaction in the intermediate **2**. In contrast to reaction **R1** cleavage of the RuC_a and C_bC_c bonds takes place before the TS, where the reaction complex is moving uphill on the potential energy surface. Therefore the cleavage process of these bonds requires energy to proceed, which contributes to the activation energy of this reaction, i.e. alleviating the cleavage will lower the barrier height of reaction **R2**. Based on the CCSD(T) calculations shown in Table 1, the activation free energy of reaction **R1** is smaller than that of reaction **R2** (G^a values of 8.5 and 11.7 kcal/mol, respectively), which is consistent with the mechanism of both reactions described above. In reaction **R1** the bond formation process takes place after the TS, however in reaction **R2** before. All chemical events along the reaction path, which occur before the TS contribute to the TS energy, therefore the activation energy of the reaction **R2** is larger because it involves energy consuming bond cleavage processes.This shows how the URVA analysis can decode which processes to modify in order to lower the reaction barrier. URVA also reveals for both reactions **R1** and **R2** a supporting contribution from the RuC_b bond representing an agostic interaction with the metal, clearly indicating the importance of this interaction for the intermediate metallacyclobutanes.

Figures 7e and 7f show the reaction path curvature profiles and curvature decompositions of reactions **R3** and **R4**, which show similar patterns as found for reactions **R1** and **R2**, although they have a different orientation of trichlorovinylsilane relative to the ethylidine group. Reaction **R3** starts from **4** and ends at intermediate **5** where the two new RuC_c and C_aC_b are formed. Similarly, as in reaction **R1**, both chemical bonds are formed in **R3** in a concerted way after the TS, which is indicated by supporting contributions of the C_aC_b bond (blue line) and the RuC_c bond (violet line) in phase 5. In the same phase we observe resisting contributions from the RuC_a bond (red line) and the C_bC_c bond (green line), and supporting contribution from the RuC_b bond (maroon line). The pre–chemical phases of reaction **R3** which are less pronounced than for reaction **R1** are dominated by the $PRuC_aC_e$ component (orange line), which is related by the rotation of the ethylidine group around the RuC_a bond. Reaction **R4** starts from intermediate **5** and forms the final product **6**. Similar as in the reaction **R2**, there are two supporting curvature contributions from the RuC_a bond (red line) and the C_bC_c bond (green line), which are cleaved in a concerted way before the TS as well as a supporting contribution from the agostic bond RuC_b (maroon line). In the same chemical phase the RuC_c bond (violet line) and the C_aC_b bond (blue line) are changing their characters from single to double bonds with resisting contributions to the reaction curvature. It is interesting to note the presence of a large resisting contribution from a $ClSiC_c$ angle component of the trichlorosilane group (brown line) in this phase, indicating on a participation of this particular group in the formation of the final product. The mechanism of both reactions is consistent with the energetics of these reactions shown in Table 1. According to Table 1 the activation free energy of the reaction **R3** is smaller than in the reaction **R4** (G^a values of 6.0 and 9.4 kcal/mol, respectively), which is consistent with the mechanism of the reaction **R4**, where the cleavage process of both chemical bonds takes place before the TS, thus contributing the energy

---

barrier.

Figure 7b shows the total NBO charge of Cat and Mol along the reaction path, where the vertical broken lines indicate the range of the all chemical phases in the reactions **R1** – **R4**. According to Figure 7b, the reaction **R1** has a larger charge separation between Cat and Mol (red lines) in the entrance channel than treaction **R2** (blue lines), which according to Table 1 correlates with the smaller activation free energy of reaction **R1** than that found in **R2** (G^a values of 8.5 and 11.7 kcal/mol, respectively). The same correlation is observed for reactions **R3** and **R4**. The Cat and Mol charge separation in reaction **R3** (green lines) in the entrance channel is larger than that in the reaction **R4** (violet lines), which correlates with the activation free energies of these two reactions (G^a values of 6.0 and 9.4 kcal/mol, respectively). Therefore we can conclude for the reactions in this series that a smaller activation energy of the reactions is related to a larger charge separation between Cat and Mol, providing a larger transfer of electron density from the catalyst to the reactants, and moving the bond formation process after the TS.

Figure 8a shows the energy profiles of reactions **R5** – **R8**, which are catalyzed by the NHC model catalyst **M2**. The NBO charges along the reaction paths of these reactions for Cat and Mol, are shown in Figure 8b, and the reaction path curvature profiles including the reaction path decomposition into internal components related to the target bonds are shown in Figures 8c – 8f. Reaction **R5** starts from reaction complex **7** ending with intermediate **8** and the intermediate formation of the two C_aC_b and RuC_c bonds. According to Figure 8c, formation of these two bonds takes place in phase 5 just after TS in a concerted way. The RuC_a and C_bC_c bond components are resisting this process indicated by their negative values whereas the RuC_b bond component is supporting. Again, the formation of the RuC_a and C_bC_c bonds takes place after the TS, therefore this process does not contribute to the reaction barrier. According to Figure 8c, the dihedral $C_eC_aRuC_f$ angle has a relatively large contribution to the curvature maxima in phases 1 and 4, which indicates that the rotation around the bond RuC_a contributes to the energy barrier. According to Figure 8d, reaction **R6** transforms reaction intermediate **8** into the final product **9** via RuC_a and C_bC_c bond cleavage, which takes place in a concerted way in phase 6 before the TS. As in reaction **R5** the RuC_c and C_aC_b bonds resist and the RuC_b bond supports bond breaking in this phase. The activation energy of this reaction is relatively high because the concerted bond breaking process takes place before the TS, which requires energy to proceed, in addition to conformational changes of the NHC ligand, as indicated by the dihedral angles NC_gC_hN and $C_fNC_gC_h$ components. Both dihedral angles are related to the puckering of the NHC ligand, which changes the interaction between the ligand and Ru, also increasing the energy barrier of this reactions (see Figure 8d). The curvature patterns of reactions **R7** and **R8** are similar to those of reactions **R5** and **R6**, although the orientation of the chlorolsiliane group relative to the ethylidene group is opposite. According to Figure 8e, in reaction **R7** the concerted formation of the two C_aC_b and RuC_c bonds takes place in phase 6 after the TS, with a resisting contribution of the RuC_a and C_bC_c bonds, similar as in reaction **R5**. The two dihedral angles $C_eC_aRuC_f$, and $C_eC_aC_bC_c$ with larger contributions in the pre–chemical phases are responsible for the correct orientation of the reacting groups. In reaction **R8**, the cleavage process of the bonds RuC_a and C_bC_c proceeds in a concerted way before the TS, with a resisting contribution of the RuC_c and C_aC_b bonds, and a contribution of two RuC_fNC_h and RuC_fNC_g dihedral angles, which are related to a puckering of the NHC ligand, causing the relatively high energy barrier.

Figure 8b presents the change for the NBO charges of Cat and Mol atoms for reactions **R5** – **R8**. According to Table 1 the activation free energy of the reaction **R5** is smaller than that for **R6** (G^a values of 8.5 and 12.8 kcal/mol, respectively), which according to Figure 8b, correlates with a larger charge separation between Cat and Mol in the entrance channel of this reaction. The same correlation is observed for reactions **R7** and **R8**. The charge separation in reaction **R7** in the entrance channel is larger than that in reaction **R8**, and the activation free energies of reaction **R7** is smaller than that in **R8** (G^a values of 4.3 and 10.5 kcal/mol, respectively). Therefore we can conclude again for the reactions in this series that a smaller activation energy is related by a larger charge separation between Cat and Mol. The larger charge separation between the reacting species generates a larger electron density transfer from the catalyst to the reactants, which moves the bond breaking process into the exit channel and lowers the activation energy.

Figures 9a – 9f summarize the results of the URVA analysis for reactions **R9** – **R12**, which are catalyzed by the NHC model catalyst **M3** with two methyl groups. Energy profiles are shown in Figure 9a, and change of the NBO charges for Cat and Mol along the reaction paths are shown in Figure 9b. The reaction path curvature profiles and the reaction path curvature decompositions into selected internal components related to the target bonds are shown in Figures 9c – 9f. According to Figure 9c, reaction **R9** starts from reaction complex **13** and ends with intermediate **14** with the two target bonds RuC_c and C_aC_b being created. Formation of these two bonds takes place in phase 7, which is indicated by supporting contributions to the reaction curvature from the internal components related to these two bond. Similar as in the reaction **R5**, formation of these bonds is accompanied by resisting contributions from the
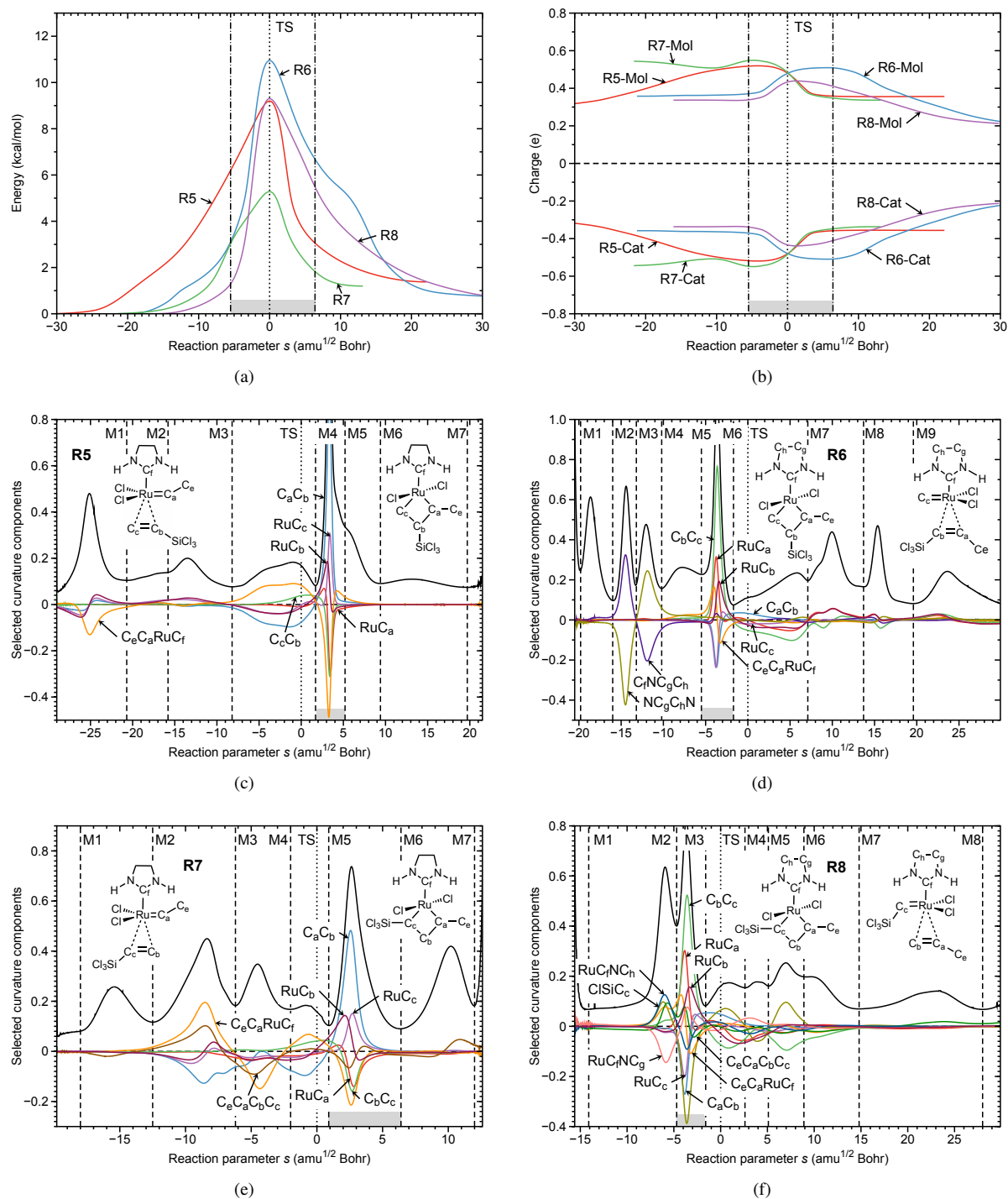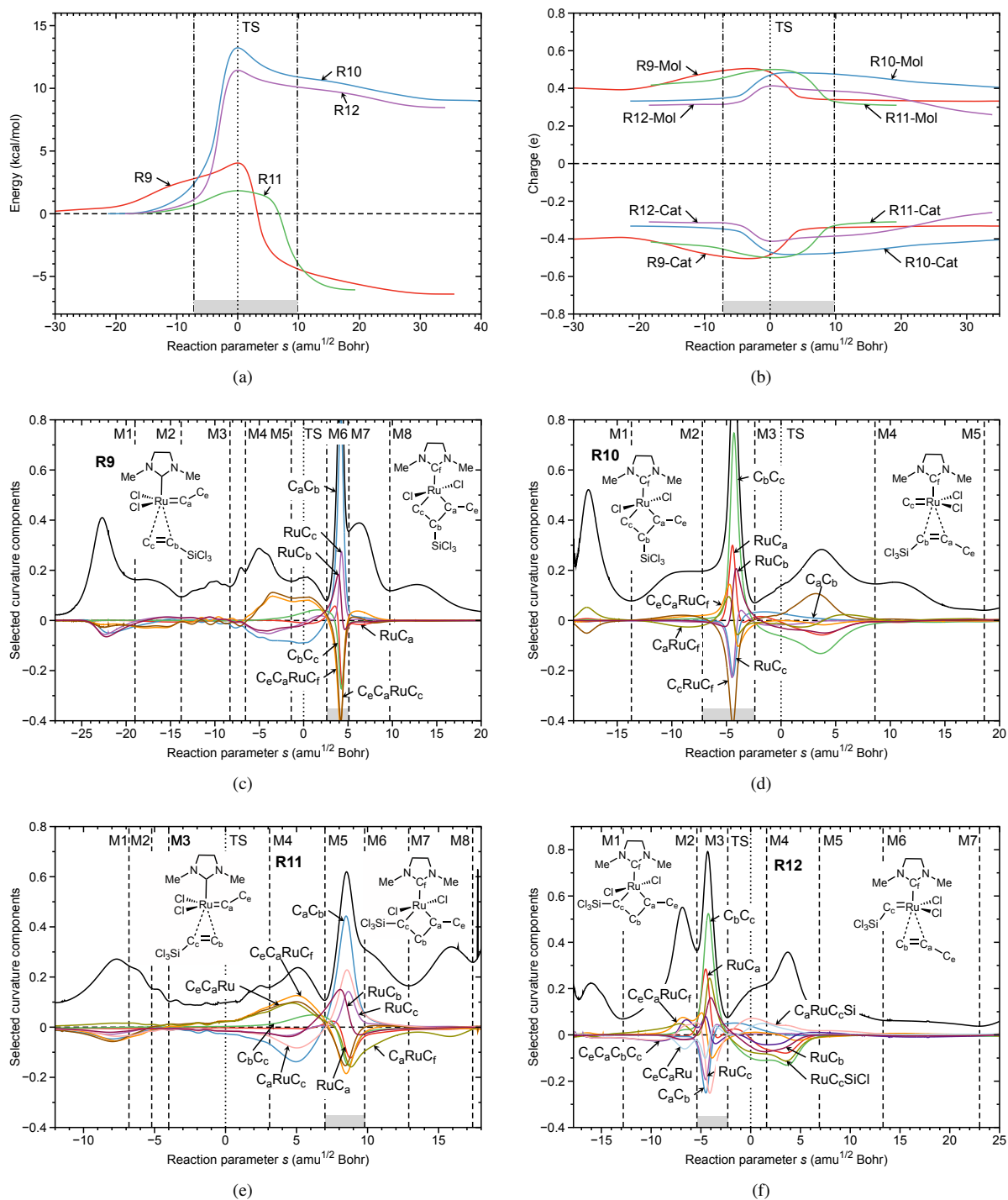
Figure 8: a) The energy profiles of the reactions **R5 – R8**. b) The charge of the catalyst (Cat) and the reactants (Mol) of the reactions **R5 – R8** . The decomposition of the curvature into internal components: c) for the reaction **R5**; d) for the reaction **R6**; e) for the reaction **R7**; f) for the reaction **R8**. Only selected hydrogen atoms are indicated. The curvature minima are shown as broken vertical lines and are labeled as M1, M2, and so on. The chemical phases where the bonds are formed/cleaved, are indicated by a gray bar. The position of TS is indicated as a dotted line, and the vertical dash–dotted lines show the range of the chemical phases.The B3LYP/6–31G(d,p)/SDD(Ru) level of theory.

Figure 9: a) The energy profiles of the reactions **R9 – R12**. b) The charge of the catalyst (Cat) and the reactants (Mol) of the reactions **R9 – R12**. The decomposition of the curvature into internal components: c) for the reaction **R9**; d) for the reaction **R10**; e) for the reaction **R11**; f) for the reaction **R12**. Hydrogen atoms are omitted. The curvature minima are shown as dashed vertical lines and are labeled as M1, M2, and so on. The chemical phases where the bonds are formed/cleaved, are indicated by a gray bar. The position of TS is indicated as a dotted line, and the vertical dash–dotted lines show the range of the chemical phases. The B3LYP/6–31G(d,p)/SDD(Ru) level of theory.

RuC_a, and C_bC_c bonds, and a supporting contribution from the RuC_b bond, again al taking place in a concerted way, after the TS. We also observe in this reaction a contribution of the $C_eC_aRuC_f$ dihedral angle reflecting a rotation about the RuC_a bond accompanied with an electronic structure reorganization before and after the TS. Similar as in reaction **R5**, the chemical phase of reaction **R9**, is located after the TS, which does not require the energy to proceed leading to a relatively low energy barrier. It is interesting to notice that the activation energy of reaction **R9** is smaller than that of reaction **R5**, which can be related to the different curvature patterns with regard to the $C_eC_aRuC_f$ dihedral angle. In reaction **R5**, there is a resisting contribution of this angle to the electronic structure change of the reaction complex in the entrance channel in phase 1. However in the entrance channel of reaction **R9**, we observe only a supporting contribution of this angle before the TS. The flexibility of the RuC_a rotational angle is related to the presence of the methyl groups in the NHC ligand of the catalyst, which decreases the activation energy by steric interactions with the C_a and C_c carbons, which will be discussed in the next section. The next reaction **R10** forms the final product **15** by breaking the RuC_a and C_bC_c bonds . According to Figure 9d, the concerted bond breaking process takes place in phase 3, involving the RuC_c and C_aC_b bonds and the agostic RuC_b bond. There are only small contributions of the two C_aRuC_f and RuC_cC_f angles in the entrance channel of reaction **R10**. The actual bond breaking processes are located before the TS, which increases the activation energy of this reaction relative to that of reaction **R9**. The activation energy of the reaction **R10** is slightly larger than the activation energy of the corresponding reaction **R6** showing the influence of the methyl groups on the energy barrier caused by steric interactions with carbons C_a and C_c, suggesting that bulkier groups such as iso-propyl, should lead to further reduction of the energy barrier.

The last two paths involve reactions **R11** and **R12**. The curvature profiles and the curvature decomposition into selected components related to the target bonds are shown in Figures 9e – 9f. Reaction **R11** starts from reaction complex **16** and ends at intermediate **17** forming the RuC_c and C_aC_b bonds, with a supporting contribution from the RuC_b bond. As in reaction **R9**, the concerted bond formation process takes place with resisting contributions of the RuC_a and C_bC_c bonds after the TS, not directly influencing the reaction barrier. The bond formation process is preceded by supporting contributions of the $C_eC_aRuC_f$ torsional angle and the C_eC_aRu bond angle, which are responsible for a correct orientation of the reacting groups. The flexibility of these two angles is related to the steric interactions between the methyl groups of NHC ligand with the target carbon atoms, which influences the energy barrier. Reaction **R12** starts with intermediate **17** and forms the final product **18** by breaking the RuC_a and C_bC_c bonds, with a supporting contribution from the RuC_b bond and resisting contributions from the RuC_c and C_aC_b in phase 3. As in reaction **R8** the bond breaking process takes place in a concerted way, before the TS, increasing the energy barrier of this reaction relative to **R8**, being also influenced by the steric interaction between the methyl groups of NHC and the carbon atoms C_a and C_c, influencing the energy barrier of this reaction.

Figure 9b presents the NBO charge change for Cat and Mol in reactions **R9** – **R12**, which are similar to the charge changes in reactions **R5** – **R8**. According to Figure 9b, reaction **R9** has a larger charge separation between Cat and Mol in before the TS, than reaction **R10**, which is reflected by a smaller activation free energy of **9** (G^a values of 2.4 and 17.1 kcal/mol, respectively). Similarly, reaction **R11**, has a larger charge separation than reaction **R12**, and a smaller activation free energy (G^a values of 5.6 and 13.1 kcal/mol, respectively). Generally we can conclude, that as in reactions **R1** and **R3** with catalyst **M1** and in reactions **R5** and **R7** with catalyst **M2**, charge separation in reactions **R9** and **R11** before the TS decreases the activation energy, supporting the transfer of the electron density from the catalyst to the reactants, and moving the bond formation process after the TS.

4.4. Interactions in the M3 Catalyst

In the following we will discuss in some more detail the influence of substituting the N–H hydrogen atoms of the NHC ligand in catalyst **M2** with more bulky methyl groups which obviously leads to a significant change in the activation energies. The activation energies of the target bond forming reactions **R9** and **R11** with catalyst **M3** (G^a values of 2.4 and 5.6 kcal/mol, respectively) become significantly smaller than those of reactions **R5** and **R7** with catalyst **M2** (G^a values of 8.5 and 4.3 kcal/mol, respectively). However, the activation energies of the target bond cleaving reactions **R10** and **R12** with catalyst **M3** (G^a values of 17.1 and 13.1 kcal/mol, respectively) become larger than their **M2** counterparts **R6** and **R8** (G^a values of 12.8 and 10.5 kcal/mol). The hydrogen atoms of the NHC methyl groups in **M3** can interact with the carbon atoms C_a and C_c of the reactants, leading to these differences in the activation energies, as also reflected in the reaction path curvature decomposition plots discussed above. Using LMA we calculated local mode force constants and frequencies of these specific interaction for all stationary points of reactions **R9** – **R12**. The results of our calculations are presented in Table 8 including also the interaction distances. According to Table 8 the local mode force constant of the interaction $H \cdots C_a$ between the C_a atom and the closest H

Table 8
Interaction distance d, local mode force constant k^a, local mode frequency ω^a for the interaction between the H atoms of the NHC methyl groups and C_a and C_c atoms for reactions **R9** – **R12**. For C atoms labeling see Figure 3. B3LYP/6–31G(d,p)/NESC/Jorge–TZP–DKH(Ru) level of theory.

Reaction	Interaction	d	k^a	ω^a	Reaction	Interaction	d	k^a	ω^a
		Å	mDyn/Å	cm^{-1}			Å	mDyn/Å	cm^{-1}
R9					**R11**				
13	H⋯C_a	2.5445	0.083	390.01	**16**	H⋯C_a	2.4321	0.124	475.14
TS(13,14)	H⋯C_a	2.5948	0.058	324.75	**TS(16,17)**	H⋯C_a	2.5625	0.063	338.59
14	H⋯C_a	3.0361	0.048	295.81	**17**	H⋯C_a	2.9063	0.066	346.07
13	H⋯C_c	3.8103	0.042	276.95	**16**	H⋯C_c	4.1623	0.083	389.74
TS(13,14)	H⋯C_c	3.3288	0.030	235.36	**TS(16,17)**	H⋯C_c	3.7489	0.054	314.26
14	H⋯C_c	3.0254	0.023	207.09	**17**	H⋯C_c	3.0459	0.061	333.31
R10					**R12**				
TS(14,15)	H⋯C_a	3.4298	0.060	331.00	**TS(17,18)**	H⋯C_a	3.3114	0.049	298.76
15	H⋯C_a	3.4225	0.066	347.32	**18**	H⋯C_a	4.0756	0.025	213.46
TS(14,15)	H⋯C_c	2.7802	0.044	283.68	**TS(17,18)**	H⋯C_c	2.6068	0.021	194.27
15	H⋯C_c	2.3774	0.045	285.33	**18**	H⋯C_c	2.4842	0.109	446.53

atom of the methyl group of reaction **R9** is largest in the reactant and becomes smaller in the TS (k^a values of 0.083 and 0.058 mDyn/Å, respectively), and the H⋯C_a distance increases (d values of 2.5445 and 2.5948 Å, respectively). The H⋯C_a interaction is a non–bonded interaction, which involves a steric repulsion between these two atoms, moving atom C_a closer to atom C_b atom thus making the bond formation process between these atoms easier. There is also a steric H⋯C_c interaction between the H atom of the other methyl group and the C_c atom, making the RuC_c bond formation more difficult. However according to Table 8 the local mode force constant of this interaction is small in the reactant and the TS (k^a values of 0.042 and 0.030 mDyn/Å, respectively), because of the large distance (d values of 3.8103 and 3.3288 Å, respectively). Therefore, the H⋯C_a interaction dominates in reaction **R9**, decreasing the energy barrier in comparison to reaction **R5** with the catalyst **M2** (G^a values of 2.4 and 8.5 kcal/mol, respectively). In the reaction **R10** the RuC_a and C_bC_c bonds are cleaved. Both steric interactions H⋯C_a and H⋯C_c make the breaking process more difficult. The local mode force constant of the H⋯C_a interaction becomes larger going from the reactant to the TS (k^a value of 0.048 and 0.060 mDyn/Å, respectively), whereas the H⋯C_a distance becomes larger as well (d values of 3.0361 and 3.4298 Å, respectively). The local mode force constant of the H⋯C_c interaction becomes also larger going from the reactant to the TS (k^a value of 0.023 and 0.044 mDyn/Å, respectively), whereas the H⋯C_c distance decreases (d values of 3.0254 and 2.7802 Å, respectively). This is another example that a stronger interaction is not necessarily a shorter interaction []. Overall, both the H⋯C_a and the H⋯C_c interactions increase the energy barrier of reaction **R10** compared to reaction **R6** with the catalyst **M2** (G^a value of 17.1 and 12.8 kcal/mol, respectively).

In reaction **R11**, the H⋯C_a interaction between the C_a atom and the closest H atom of the methyl is larger in the reactant than in the TS (k^a values of 0.124 and 0.063 mDyn/Å, respectively), whereas the distance is increasing (d value of 2.4321 and 2.5625 Å, respectively). Similarly, the H⋯C_c interaction becomes smaller from the reactant to the TS (k^a values of 0.083 and 0.054 mDyn/Å, respectively) with a decreasing distance (d value of 4.1623 and 3.7489 Å, respectively). Although the interaction H⋯C_a dominates, the activation free energy of reaction **R11** is larger than in reaction **R7** with the catalyst **M2** (G^a values of 5.6 and 4.3 kcal/mol, respectively), which indicates that there are additional decisive interactions, which are related to the position of the trichlorosilane group in these two reactions. Similar as in reaction **R10**, in reaction **R12** the RuC_a and C_bC_c bonds are cleaved, and both steric H⋯C_a and H⋯C_c interactions make the breaking process more difficult. The local mode force constant of the H⋯C_a interactions is decreasing from the reactant to the TS (k^a values of 0.066 and 0.049 mDyn/Å, respectively) and its distance is increasing (d values of 2.9063 and 3.3114 Å, respectively). The strength of the H⋯C_c interactions is decreasing (k^a values of 0.061 and 0.021 mDyn/Å, respectively), however its distance is decreasing as well (d value of 3.0459 and 2.6068 Å, respectively). The overall effect of both interactions makes the energy barrier of this reaction larger relative to reaction **R8** with catalyst **M2** (G^a value of 13.1 and 10.5 kcal/mol, respectively).

Table 9
Rotational angle α ($C_e C_a RuC_f$), local mode force constant k^a, local mode frequency ω^a for the torsional rotation around the RuC_a bond in reactions **R5**, **R7**, **R9**, and **R11**. Δ – difference between TS and Re. For C atoms labeling see Figure 3. B3LYP/6–31G(d,p)/NESC/Jorge–TZP–DKH(Ru) level of theory.

Reaction	α	k^a	ω^a	Reaction	α	k^a	ω^a
	Deg	mDynÅ/Rad^2	cm^{-1}		Deg	mDynÅ/Rad^2	cm^{-1}
R5				**R9**			
7	-3.22	0.050	153.59	**13**	-36.61	0.169	259.93
TS(7,8)	-73.42	0.192	278.49	**TS(13,14)**	-80.71	0.100	203.17
8	-65.33	0.312	374.33	**14**	-67.55	0.217	317.28
Δ	-70.20	0.142	124.90	Δ	-44.10	-0.069	-56.76
R7				**R11**			
10	-147.14	0.074	167.05	**16**	-38.52	0.167	265.66
TS(10,11)	-85.28	0.156	254.86	**TS(16,17)**	-70.85	0.189	281.49
11	-68.73	0.230	331.88	**17**	-67.56	0.186	298.16
Δ	61.87	0.082	87.81	Δ	-32.33	0.022	15.83

Using LMA we have also analyzed the strength of the local mode related to the torsional rotation around the RuC_a bond, which involves atoms $C_e C_a RuC_f$, for reactions **R5** and **R7** with catalyst **M2** and for reactions **R9** and **R11** with catalyst **M3**. The results of our analysis are presented in Table 9. We observe a relative large rotation around this bond going from the reactant to the TS in reactions **R5** and **R7** ($\Delta\alpha$ values of -70.20, and 61.87 Deg, respectively), which are also changing directions. In both reactions, the local mode force constant is increasing from a relative small value in the reactant to a larger value in the TS (Δk^a values of 0.142 and 0.082 mDynÅ/Rad^2, for **R5** and **R7**, respectively). The large Δk^a value in the reaction **R5** correlates with a larger energy barrier relative to reaction **R7** (G^a values of 8.5 and 4.3 kcal/mol, respectively), indicating that decreased flexibility of this rotation at the TS correlates with an increased activation energy. For reactions **R9** and **R11** with the **M3** catalyst, this angle is changing monotonically in the same direction ($\Delta\alpha$ values of -44.10 and -32.33 Deg, respectively) and $\Delta\alpha$ values are much smaller than in reactions **R5** and **R7**. We also observe that the local mode force constant in reactions **R9** and **R11** is changing from a larger to a smaller value (Δk^a values of -0.069 and 0.022 mDynÅ/Rad^2, respectively), making this rotation more flexible at the TS, which leads to a smaller activation energy (G^a values of 2.4 and 5.6 kcal/mol, respectively) compared with reactions **R5** and **R7** (G^a values of 8.5 and 4.3 kcal/mol, respectively). Generally we can conclude that both changes in the torsional angle $\Delta\alpha$ and the local mode force constant Δk^a correlate for some extend with the energy barriers, suggesting a contribution of RuC_a bond rotation to the reaction energetics of these reaction. LMA also provides an insight into a larger stabilization of the metallacyclobutane intermediate **14** relative to intermediate **17**. According to Table 6 the local mode force constant of the RuC_c bond in **14** has a value of 2.609 mDyn/Å, and according to Table 7 this same bond in **17** has a strength of 2.339 mDyn/Å, which indicates that the presence of the chlorosilane group at the carbon C_c in **17** decreases the RuC_c bond strength, destabilizing this intermediate relative to **14**. Also the summed strength of the RuC_a, $C_a C_b$, $C_b C_c$, and RuC_c bonds in **14** is larger than in **17** (sum of k^a values: 8.687 and 8.155 mDyn/Å, respectively), indicating a stronger stabilization of **14**, which is induced by the chlorosilane group at the C_b carbon.

For both the first and second–generation Grubbs catalysts, the formation of a stable metallacyclobutane intermediate is a key element of the catalytic process, which is not fully understood yet. It has been suggested that the metallacyclobutane benefits from of a specific 4–center–2–electron interaction, coined α,β–(CCC) agostic bond with the metal [82], which donates σ–electron density to the Ru center increasing the total electron density of the 16–electron Ru core [25, 28]. It has been further suggested that this interaction mimics α and β agostic hydrogen-bonding as sketched in Figure 2. Therefore, the investigation of the intermediate metallacyclobutane and the assessment of the proposed α,β–(CCC) agostic metal-bonding was one particular focus of our study.

4.5. Agostic bonding in metallacyclobutanes

In this section we will shed more light into the suggested stabilization of the metallacyclobutane intermediates via a specific 4–center–2–electron α,β–(CCC) agostic interaction with the metal atom[82, 83, 25, 28]. As sketched in Figure 2 the RuC_b interaction plays a key role. Table 10 collects the RuC_b distance, local mode force constant and local mode frequency, bond strength order, electron and energy density at the ring critical point of the four-membered ring defined by the Ru, C_a, C_b, and C_c atoms for the metallacyclobutane intermediates **2**, **5**, **8**, **11**, **14**, and **17** investigated in this work.

Table 10

The interaction distance d, the local mode force constant k^a, the local mode frequency ω^a for the agostic interaction RuC_b for metallacyclobutane **2**, **5**, **8**, **11**, **14**, and **17**. For C atoms labeling see Figure 3. The B3LYP/6–31G(d,p)/NESC/Jorge–TZP–DKH(Ru) level of theory.

Molecule	r	k^a	ω^a	BSO	ρ(ring)	H_ρ(ring)
	Å	mDyn/Å	cm^{-1}		e/Bohr^3	Hartree/Bohr^3
2	2.2247	2.058	570.43	1.010	0.0709	-0.0104
5	2.2425	2.186	587.91	1.054	0.0701	-0.0099
8	2.2312	2.075	572.73	1.016	0.0692	-0.0091
11	2.2517	2.187	588.05	1.054	0.0682	-0.0087
14	2.2483	2.025	565.78	0.999	0.0673	-0.0082
17	2.2607	2.152	583.32	1.042	0.0671	-0.0081

According to Table 10 the strongest RuC_b interactionis observed for complexes **5** and **11** (BSO value of 1.05 and 1.05, respectively) which according to Table 1 are the reactants of reactants **R4** and **R8** with the smallest energy barriers in this series (G^a vales of 9.4 and 10.5 kcal/mol, respectively) in this series. The weakest RuC_b interaction is found for **14** (BSO value of 1.0), the reactant of reaction **R10** with the largest energy barrier (G^a value 17.1 kcal/mol). We conclude that a stronger agostic interaction, as quantified via the strength of the RuC_b bond correlates to some extend with a smaller energy barrier involving the metallacyclobutane intermediate as a reactant. The second step reactions (**R2**, **R4**, **R6**, **R8**, **R10**, and **R12**) investigated in our study have generally larger activation energies than the first step reactions (**R1**, **R3**, **R5**, **R7**, **R9**, and **R11**), because according to our URVA analysis, the bond cleavage process in the second step reactions takes place before the TS, which requires energy to move the reaction complex uphill on the potential energy surface. According to Tables 1 and 10, the energy barrier of the second step reactions can be lowered by a stronger agostic RuC_b interaction with the metal. It is also interesting to note that the RuC_b strength in **5** (reactant of reaction **R4**) is larger than in **2** (reactant of reaction **R4**), as reflected by the BSO values of 1.05 and 1.01, respectively. The difference between reactions **R4** and **R2**, is the position of the trichlorosilane relative to the ethylidene group. In reaction **R2** the trichlorosilane group is bonded to the C_b carbon atom, involved in the agostic interaction with the metal decreasing the strength of the RuC_b interaction and increasing the energy barrier (G^a values 9.4 and 11.7 kcal/mol for the reactions **R4** and **R2**, respectively). A similar correlation is observed for **11** (reactant of reaction **R8**) and **8** (reactant of reaction **R6**) with BSO values of 1.05 and 1.02; G^a values 10.5 and 12.8 respectively, as well as for **17** (reactant of reaction **R12**) and **14** (reactant of reaction **R10**) with BSO values of 1.04 and 1.0; G^a values 13.1 and 17.1 respectively.

As suggested in previous studies [25, 28, 178] the 4–center–2–electron α,β–(CCC) agostic interaction in the metallacyclobutane complexes is involved in the donation of σ–electron density from the olefin moiety and ethylidene ligand to the Ru coordination center and increases the electron density to form a 16–electron stable complex. In addition to the σ–electron donation, the α,β–(CCC) agostic interaction may also be supplemented by backbonding into the σ^* CC orbital, which can lead to easy cleavage of this bond [82]. According to Tables 2 and 10, the strength of the agostic RuC_b interaction in metallacyclobutane intermediate **2** (BSO value of 1.01) is very close to the strength the RuC_a and RuC_c bonds in **2** (BSO values of 1.06 and 1.18, respectively), with similar values observed for **5**, **8**, **11**, **14**, and **17**, which indicates on the general importance of the agostic interaction in these intermediates. Moreover, according to Table 10, all metallacyclobutane intermediates have a negative value of the energy density at the ring critical point, indicating on a dominance of the potential energy of the π–electrons in the middle of the ring [179]. According to Figures 4 – 6 the Laplacian of the electron density inside the metallacyclobutane ring is positive indicating on the π–electron charge

depletion, and becomes negative close to the carbon atoms showing a charge concentration. In summary according to Table 10 and Figures 4 – 6, we observe in our study that both π–electron concentration concentration close to the carbon atoms, and the agostic interaction with the metal facilitate CC bond cleavage, lowering the energy barrier of this process.

4.6. Conclusions

We analyzed the mechanism of the regioselective [2+2] cycloaddition and cycloreversion reactions between trichloro-vinylsilane and ethylidine coordinated to three models (**M1**, **M2** and **M3**) of the active form of the original first and second–generation Grubbs catalyst (**GI** and **GII**). **M1** used in our study is a simplified model of the first–generation Grubbs catalyst with a trimethylphosphine ligand coordinated to the Ru atom, **M2** is a simplified model of the second–generation catalyst with an unsubstituted NHC ligand, while **M3** is a model of the second–generation catalyst with a 2,5–dimethyl–NHC ligand. With two possible orientations of trichlorovinylsilane relative to the ethylidene group and two reaction steps for each reaction (i.e., *step I*: formation of a stable intermediate metallacyclobutane and *step II*: ring-opening of the intermediate cyclobutane ring forming the final product) this led to a total of 12 reactions paths, 18 minima and 12 TSs.

- In all reactions four target bonds play a key role, either being formed and/or broken or changing from double to single bonds and vice versa during the catalytic process. According to our URVA results, in all *step I* reactions investigated in this work bond formation and change from double to single bond character of the target bonds take place in a concerted way after the TS (i.e. process does not contribute to the reaction barrier); in all *step II* ring-opening reactions bond cleavage and change from single to double character also happens in a concerted way, however, before the TS (i.e. process contributes to the reaction barrier). As a consequence, all *step I* reaction have a lower the activation energies than their than *step II* counterparts. The analysis of the NBO charges along the reaction paths revealed that the *step I* reactions are characterized by a larger charge separation between the catalyst and the reacting species in the entrance channel, than the *step II* reactions. This electron density transfer from the catalyst to the reacting species further reduces the energy barrier.

- According to our results, **M3** is the most effective catalyst. Its activity is related to a strong stabilization of the metallacyclobutane intermediate and specific interactions between the reacting species and the methyl hydrogen atoms of the 2,5–di–methyl-NHC ligand of the catalyst. *Step I* reactions with the **M3** catalyst have generally lower activation energies than the corresponding reactions with the **M1** and **M2** catalysts. As revealed by our data, in *step I* reactions where the target bonds are formed, steric interactions with the methyl groups decrease the activation energy by moving the reacting carbon atoms closer together. However the price to pay is that in *step II* reactions, the NHC-methyl groups lead to on opposite effect which increases the activation energy by making bond cleavage more difficult. Therefore, when selecting other, maybe more bulky NHC substituents to facilitate the *step I* reactions one has carefully check the energetic consequences for *step II* reactions, which can be efficiently monitored and predicted by LMA.

- We could also explain the suggested role of 4–center–2–electron α,β–(CCC) agostic interactions in the met-allacyclobutane intermediate donating electron density to the Ru coordination center and facilitating CC bond cleavage taking place in the *step II* reactions, leading in this way to lower energy barriers.

Overall, the new mechanistic details obtained with the URVA and LMA analysis can serve as a roadmap for the optimization of current and the future design of the next generations of Grubbs catalysts and beyond.
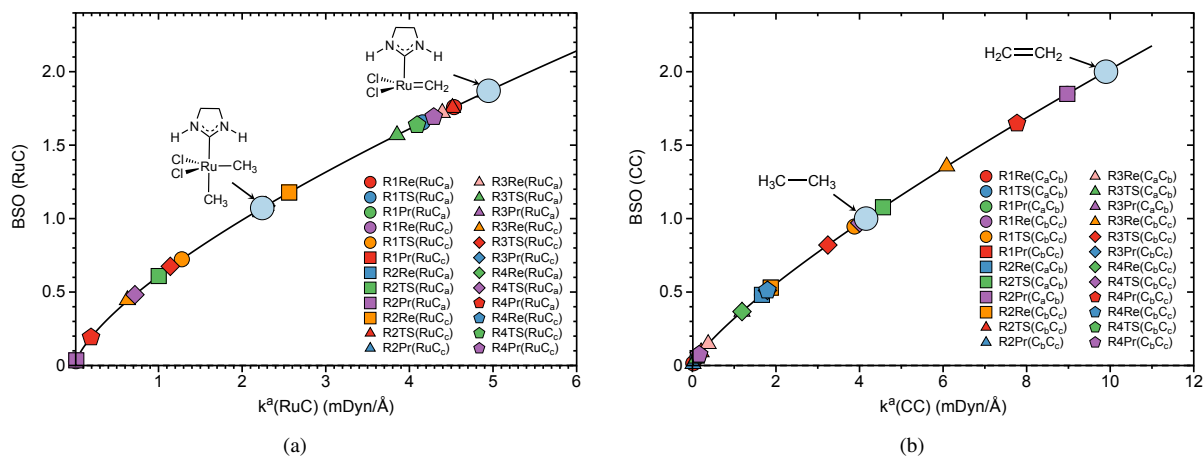
A. Appendix

Figure 10: Bond strength order BSO as a function of local mode force constant k^a for reactions **R1 – R4**. The values for the reference molecules are indicated as light blue circles. Only selected hydrogen atoms are indicated. Re – reactant, TS – transition state, Pr – product. For bond labeling see Figure 3. B3LYP/6–31G(d,p)/NESC/Jorge–TZP–DKH(Ru) level of theory. a) RuC bonds; b) The CC bonds.
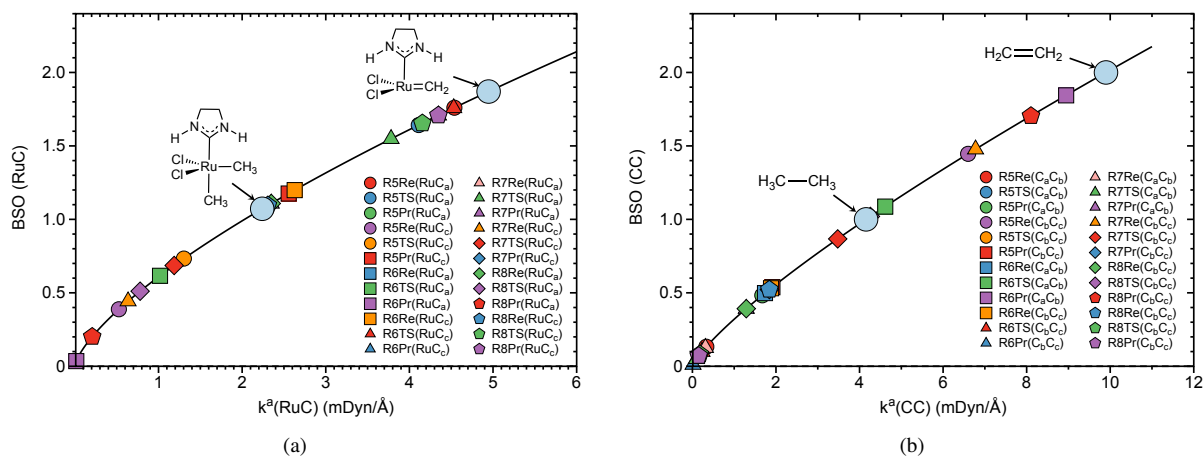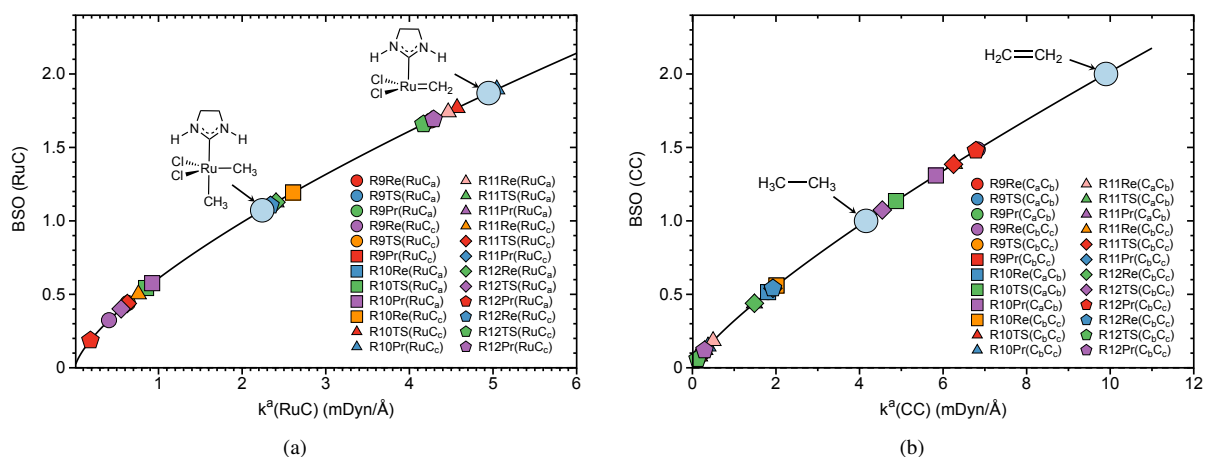

Figure 11: Bond strength order BSO as a function of local mode force constant k^a for the reactions **R5 – R8**. The values for the reference molecules are indicated as light blue circles. Only selected hydrogen atoms are indicated. Re – reactant, TS – transition state, Pr – product. For bond labeling see Figure 3. B3LYP/6–31G(d,p)/NESC/Jorge–TZP–DKH(Ru) level of theory. a) RuC bonds; b) CC bonds.

Figure 12: Bond strength order BSO as a function of local mode force constant k^a for the reactions **R9 – R12**. The values for the reference molecules are indicated as light blue circles. Only selected hydrogen atoms are indicated. Re – reactant, TS – transition state, Pr – product. For bond labeling see Figure 3. B3LYP/6–31G(d,p)/NESC/Jorge–TZP–DKH(Ru) level of theory. a) RuC bonds; b) CC bonds.

References

[1] O. M. Ogba, N. C. Warner, D. J. O'Leary, R. H. Grubbs, Recent advances in ruthenium–based olefin metathesis, Chem. Soc. Rev. 47 (2018) 4510–4544.

[2] C. K. Chu, T.-P. Lin, H. Shao, A. L. Liberman-Martin, P. Liu, R. H. Grubbs, Disentangling ligand effects on metathesis catalyst activity: Experimental and computational studies of ruthenium–aminophosphine complexes, J. Am. Chem. Soc. 140 (2018) 5634–5643.

[3] T. P. Montgomery, A. M. Johns, R. H. Grubbs, Recent advancements in stereoselective olefin metathesis using ruthenium catalysts, Catalysts 7 (2017) 87–123.

[4] K. M. Engle, G. Lu, S.-X. Luo, L. M. Henling, M. K. Takase, P. Liu, K. N. Houk, R. H. Grubbs, Origins of initiation rate differences in ruthenium olefin metathesis catalysts containing chelating benzylidenes, J. Am. Chem. Soc. 137 (2015) 5782–5792.

[5] G. C. Vougioukalakis, R. H. Grubbs, Ruthenium–based heterocyclic carbene-coordinated olefin metathesis catalysts, Chem. Rev. 110 (2010) 1746–1787.

[6] S. H. Hong, R. H. Grubbs, Highly active water–soluble olefin metathesis catalyst, J. Am. Chem. Soc. 128 (2006) 3508–3509.

[7] S. B. Garber, J. S. Kingsbury, B. L. Gray, A. H. Hoveyda, Efficient and recyclable monomeric and dendritic Ru–based metathesis catalysts, J. Am. Chem. Soc. 122 (2000) 8168–8179.

[8] M. S. Sanford, J. A. Love, R. H. Grubbs, Mechanism and activity of ruthenium olefin metathesis catalysts, J. Am. Chem. Soc. 123 (2001) 6543–6554.

[9] J. A. Love, J. P. Morgan, T. M. Trnka, R. H. Grubbs, A practical and highly active ruthenium–based catalyst that effects the cross metathesis of acrylonitrile, Angew. Chem. Int. Ed. 41 (2002) 4035–4037.

[10] P. Schwab, M. B. France, J. W. Ziller, R. H. Grubbs, A series of wel—defined metathesis catalysts–synthesis of [RuCl$_2$(CHR')(PR$_3$)$_2$] and its reactions, Angew. Chem. Int. Ed. 34 (1995) 2039–2041.

[11] E. L. Dias, S. T. Nguyen, R. H. Grubbs, Well–defined ruthenium olefin metathesis catalysts: Mechanism and activity, J. Am. Chem. Soc. 119 (1997) 3887–3897.

[12] M. Scholl, T. M. Trnka, J. P. Morgan, R. H. Grubbs, Increased ring closing metathesis activity of ruthenium–based olefin metathesis catalysts coordinated with imidazolin–2–ylidene ligands, Tetrahed. Lett. 40 (1999) 2247–2250.

[13] S. T. Nguyen, L. K. Johnson, R. H. Grubbs, J. W. Ziller, Ring–opening metathesis polymerization (ROMP) of norbornene by a group VIII carbene complex in protic media, J. Am. Chem. Soc. 114 (1992) 3974–3975.

[14] M. Jawiczuk, A. Marczyk, B. Trzaskowski, Decomposition of ruthenium olefin metathesis catalyst, Catalysts 10 (2020) 887:1–56.

[15] C. S. Higman, J. A. M. Lummiss, D. E. Fogg, Olefin metathesis at the dawn of implementation in pharmaceutical and specialty–chemicals manufacturing, Angew. Chem. Int. Ed. 55 (2016) 3552–3565.

[16] D. Hughes, P. Wheeler, D. Ene, Olefin metathesis in drug discovery and development–examples from recent patent literature, Org. Proc. Res. Develop. 21 (2017) 1938–1962.

[17] M. Yu, S. Lou, F. Gonzalez-Bobes, Ring-closing metathesis in pharmaceutical development: Fundamentals, applications, and future directions, Org. Proc. Res. Develop. 22 (2018) 918–946.

[18] A. C. Flick, C. A. Leverett, H. X. Ding, E. McInturff, S. J. Fink, C. J. Helal, C. J. O'Donnell, Synthetic approaches to the new drugs approved during 2017, J. Med. Chem. 62 (2019) 7340–7382.

[19] G. Turczel, E. Kovács, G. Merza, P. Coish, P. T. Anastas, R. Tuba, Synthesis of semiochemicals via olefin metathesis, ACS Sust. Chem. Eng. 7 (2019) 33–48.

[20] S. Chikkali, S. Mecking, Refining of plant oils to chemicals by olefin metathesis, Angew. Chem. Int. Ed. 51 (2012) 5802–5808.

[21] M. Winkler, M. A. R. Meier, Olefin cross–metathesis as a valuable tool for the preparation of renewable polyesters and polyamides from unsaturated fatty acid esters and carbamates, Green Chem. 16 (2014) 3335–3340.

[22] P. Vignon, T. Vancompernolle, J.-L. Couturier, J.-L. Dubois, A. Mortreux, R. M. Gauvin, Cross–metathesis of biosourced fatty acid derivatives: A step further toward improved reactivity, ChemSusChem 8 (2015) 1143–1146.

[23] J.-L. P. Hérisson, Y. Chauvin, Catalyse de transformation des oléfines par les complexes du tungstène. II. télomérisation des oléfines cycliques en présence d'oléfines acycliques, Makromol. Chem. 141 (1971) 161–176.

[24] L. Cavallo, Mechanism of ruthenium–catalyzed olefin metathesis reactions from a theoretical perspective, J. Am. Chem. Soc. 124 (2002) 8965–8973.

[25] C. H. Suresh, N. Koga, Orbital interactions in the ruthenium olefin metathesis catalysts, Organometallics 23 (2004) 76–80.

[26] C. Adlhart, P. Chen, Mechanism and activity of ruthenium olefin metathesis catalysts: The role of ligands and substrates from a theoretical perspective, J. Am. Chem. Soc. 126 (2004) 3496–3510.

[27] W. J. van Rensburg, P. J. Steynberg, W. H. Meyer, M. M. Kirk, G. S. Forman, DFT prediction and experimental observation of substrate–induced catalyst decomposition in ruthenium–catalyzed olefin metathesis, J. Am. Chem. Soc. 126 (2004) 14332–14333.

[28] C. H. Suresh, M.-H. Baik, α,β(C–C–C) agostic bonds in transition metal based olefin metathesis catalyses, Dalton Trans. (2005) 2982–2984.

[29] S. F. Vyboishchikov, W. Thiel, Ring–closing olefin metathesis on ruthenium carbene complexes: Model DFT study of stereochemistry, Chem. Eur. J. 11 (2005) 3921–3935.

[30] A. C. Tsipis, A. G. Orpen, J. N. Harvey, Substituent effects and the mechanism of alkene metathesis catalyzed by ruthenium dichloride catalysts, Dalton Trans. (2005) 2849–2858.

[31] W. J. van Rensburg, P. J. Steynberg, M. M. Kirk, W. H. Meyer, G. S. Forman, Mechanistic comparison of ruthenium olefin metathesis catalysts: DFT insight into relative reactivity and decomposition behavior, J. Organomet. Chem. 691 (2006) 5312–5325.

[32] D. Benitez, E. Tkatchouk, W. A. Goddard, Conformational analysis of olefin–carbene ruthenium metathesis catalysts, Organometallics 28 (2009) 2643–2645.

[33] H. Clavier, A. Correa, E. C. Escudero-Adán, J. Benet-Buchholz, L. Cavallo, S. P. Nolan, Chemodivergent metathesis of dienynes catalyzed by ruthenium–indenylidene complexes: An experimental and computational study, Chem. Europ. J. 15 (2009) 10244–10254.

[34] P. Śliwa, J. Handzlik, Assessment of density functional methods for the study of olefin metathesis catalysed by ruthenium alkylidene com-

plexes, Chem. Phys. Lett. 493 (2010) 273–278.

[35] S. Fomine, M. A. Tlenkopatchev, Computational modeling of renewable molecules. ruthenium alkylidene–mediated metathesis of trialkyl–substituted olefins, Organometallics 29 (2010) 1580–1587.

[36] N. Bahri-Laleh, R. Credendino, L. Cavallo, The intriguing modeling of cis–trans selectivity in ruthenium–catalyzed olefin metathesis, Beilstein J. Org. Chem. 7 (2011) 40–45.

[37] R. Credendino, A. Poater, F. Ragone, L. Cavallo, A computational perspective of olefins metathesis catalyzed by N–heterocyclic carbene ruthenium (pre)catalysts, Cat. Sci. Tech. 1 (2011) 1287–1297.

[38] J. Mathew, C. H. Suresh, Assessment of stereoelectronic effects in Grubbs first–generation olefin metathesis catalysis using molecular electrostatic potential, Organometallics 30 (2011) 1438–1444.

[39] J. Mathew, C. H. Suresh, Assessment of steric and electronic effects of N–Heterocyclic carbenes in Grubbs olefin metathesis using molecular electrostatic potential, Organometallics 30 (2011) 3106–3112.

[40] P. Liu, X. Xu, X. Dong, B. K. Keitz, M. B. Herbert, R. H. Grubbs, K. N. Houk, Z–selectivity in olefin metathesis with chelated ru catalysts: Computational studies of mechanism and selectivity, J. Am. Chem. Soc. 134 (2012) 1464–1467.

[41] Y. Minenkov, G. Occhipinti, W. Heyndrickx, V. R. Jensen, The nature of the barrier to phosphane dissociation from Grubbs olefin metathesis catalysts, Eur. J. Inorg. Chem. 2012 (2012) 1507–1516.

[42] F. Nuñez-Zarur, X. Solans-Monfort, L. Rodriguez-Santiago, M. Sodupe, Differences in the activation processes of phosphine–containing and Grubbs–Hoveyda–type alkene metathesis catalysts, Organometallics 31 (2012) 4203–4215.

[43] J. I. du Toit, C. G. C. E. van Sittert, H. C. M. Vosloo, Metal carbenes in homogeneous alkene metathesis: Computational investigations, J. Organomet. Chem. 738 (2013) 76–91.

[44] B. Trzaskowski, K. Grela, Structural and mechanistic basis of the fast metathesis initiation by a six–coordinated ruthenium catalyst, Organometallics 32 (2013) 3625–3630.

[45] Y. Minenkov, G. Occhipinti, V. R. Jensen, Complete reaction pathway of ruthenium–catalyzed olefin metathesis of ethyl vinyl ether: Kinetics and mechanistic insight from DFT, Organometallics 32 (2013) 2099–2111.

[46] C. A. Urbina-Blanco, A. Poater, T. Lebl, S. Manzini, A. M. Z. Slawin, L. Cavallo, S. P. Nolan, The activation mechanism of Ru–indenylidene complexes in olefin metathesis, J. Am. Chem. Soc. 135 (2013) 7073–7079.

[47] K. Paredes-Gil, X. Solans-Monfort, L. Rodriguez-Santiago, M. Sodupe, P. Jaque, DFT study on the relative stabilities of substituted ruthenacyclobutane intermediates involved in olefin cross–metathesis reactions and their interconversion pathways, Organometallics 33 (2014) 6065–6075.

[48] S. Vummaleti, L. Cavallo, A. Poater, The driving force role of ruthenacyclobutanes., Theor. Chem. Acc. 134 (2015) 1–6.

[49] A. Poater, L. Cavallo, A comprehensive study of olefin metathesis catalyzed by Ru–based catalysts, Beilstein J. Org. Chem. 11 (2015) 1767–1780.

[50] P. Śliwa, K. Kurleto, J. Handzlik, S. Rogalski, P. Żak, B. Wyrzykiewicz, C. Pietraszuk, Regioselectivity of stoichiometric metathesis of vinylsilanes with second–generation Grubbs catalyst: A combined DFT and experimental study, Organometallics 35 (2016) 621–628.

[51] J. Engel, W. Smit, M. Foscato, G. Occhipinti, K. W. Törnroos, V. R. Jensen, Loss and reformation of ruthenium alkylidene: Connecting olefin metathesis, catalyst deactivation, regeneration, and isomerization, J. Am. Chem. Soc. 139 (2017) 16609–16619.

[52] P. R. Remya, C. H. Suresh, Theoretical evidence for bond stretch isomerism in Grubbs olefin metathesis, J. Comput. Chem. 38 (2017) 1704–1711.

[53] J. M. Grandner, H. Shao, R. H. Grubbs, P. Liu, K. N. Houk, Origins of the stereoretentive mechanism of olefin metathesis with ru–dithiolate catalysts, J. Org. Chem. 82 (2017) 10595–10600.

[54] A. Zieliński, G. Szczepaniak, R. Gajda, K. Woźniak, B. Trzaskowski, D. Vidović, A. Kajetanowicz, K. Grela, Ruthenium olefin metathesis catalysts systematically modified in chelating benzylidene ether fragment: Experiment and computations, Eur. J. Inorg. Chem. 2018 (2018) 3675–3685.

[55] P. R. Remya, C. H. Suresh, Grubbs and Hoveyda–Grubbs catalysts for pyridine derivative synthesis: Probing the mechanistic pathways using DFT, Mol. Cat. 450 (2018) 29–38.

[56] P. Śliwa, M. P. Mitoraj, F. Sagan, J. Handzlik, Formation of active species from ruthenium alkylidene catalysts – an insight from computational perspective, J. Mol. Model. 25 (2019) 331.

[57] M. Jawiczuk, K. Młodzikowska-Pieńko, B. Trzaskowski, Impact of the olefin structure on the catalytic cycle and decomposition rates of Hoveyda–Grubbs metathesis catalysts, Phys. Chem. Chem. Phys. 22 (2020) 13062–13069.

[58] M. Jawiczuk, A. Marczyk, K. Młodzikowska-Pieńko, B. Trzaskowski, Impact of the carbene derivative charge on the decomposition rates of Hoveyda–Grubbs–like metathesis catalysts, J. Chem. Phys. A 124 (2020) 6158–6167.

[59] M. Jawiczuk, K. Młodzikowska-Pieńko, S. Osella, B. Trzaskowski, Molecular modeling of mechanisms of decomposition of ruthenium metathesis catalysts by acrylonitrile, Organometallics 39 (2020) 239–246.

[60] L. M. Azofra, S. V. C. Vummaleti, Z. Zhang, A. Poater, L. Cavallo, σ/π plasticity of NHCs on the ruthenium–phosphine and ruthenium–ylidene bonds in olefin metathesis catalysts, Organometallics 39 (2020) 3972–3982.

[61] K. Getty, M. U. Delgado-Jaime, P. Kennepohl, An electronic rationale for observed initiation rates in ruthenium-mediated olefin metathesis: Charge donation in phosphine and N–Heterocyclic carbene ligands, J. Am. Chem. Soc. 129 (2007) 15774–15776.

[62] N. S. Antonova, J. J. Carbó, J. M. Poblet, Quantifying the donor–acceptor properties of phosphine and N–Heterocyclic carbene ligands in Grubbs catalysts using a modified eda procedure based on orbital deletion, Organometallics 28 (2009) 4283–4287.

[63] B. F. Straub, Origin of the high activity of second–generation Grubbs catalysts, Angew. Chem. Int. Ed. 44 (2005) 5974–5978.

[64] B. F. Straub, Ligand influence on metathesis activity of ruthenium carbene catalysts: A DFT study, Adv. Synth. Catal. 349 (2007) 204–214.

[65] D. J. Nelson, S. P. Nolan, Quantifying and understanding the electronic properties of n–heterocyclic carbenes, Chem. Soc. Rev. 42 (2013) 6723–6753.

[66] L. Cavallo, A. Correa, C. Costabile, H. Jacobsen, Steric and electronic effects in the bonding of N–heterocyclic ligands to transition metals,

J. Organomet. Chem. 690 (2005) 5407–5413.

[67] R. Dorta, E. D. Stevens, N. M. Scott, C. Costabile, L. Cavallo, C. D. Hoff, S. P. Nolan, Steric and electronic properties of N-Heterocyclic carbenes (NHC): A detailed study on their interaction with Ni(CO)$_4$, J. Am. Chem. Soc. 127 (2005) 2485–2495.

[68] R. A. Kelly III, H. Clavier, S. Giudice, N. M. Scott, E. D. Stevens, J. Bordner, I. Samardjiev, C. D. Hoff, L. Cavallo, S. P. Nolan, Determination of N-Heterocyclic carbene (NHC) steric and electronic parameters using the [(NHC)Ir(CO)$_2$Cl] system, Organometallics 27 (2008) 202–210.

[69] A. R. Chianese, X. Li, M. C. Janzen, J. W. Faller, R. H. Crabtree, Rhodium and iridium complexes of N-Heterocyclic carbenes via transmetalation: Structure and dynamics, Organometallics 22 (2003) 1663–1667.

[70] D. G. Gusev, Electronic and steric parameters of 76 N-Heterocyclic carbenes in Ni(CO)$_3$(NHC), Organometallics 28 (2009) 6458–6461.

[71] N. Fey, M. F. Haddow, J. N. Harvey, C. L. McMullin, A. G. Orpen, A ligand knowledge base for carbenes (LKB-C): maps of ligand space, Dalton Trans. (2009) 8183–8196.

[72] N. Fey, The contribution of computational studies to organometallic catalysis: descriptors, mechanisms and models, Dalton Transactions 39 (2010) 296–310.

[73] J. Mathew, C. H. Suresh, Use of molecular electrostatic potential at the carbene carbon as a simple and efficient electronic parameter of N-heterocyclic carbenes, Inorg. Chem. 49 (2010) 4665–4669.

[74] G. Occhipinti, H.-R. Bjørsvik, V. R. Jensen, Quantitative structure–activity relationships of ruthenium catalysts for olefin metathesis, J. Am. Chem. Soc. 128 (2006) 6952–6964.

[75] K. B. Wiberg, Application of the Pople–Santry–Segal CNDO method to the cyclopropylcarbinyl and cyclobutyl cation and to bicyclobutane, Tetrahedron 24 (1968) 1083–1096.

[76] H. Jacobsen, A. Correa, C. Costabile, L. Cavallo, π–acidity and π–basicity of N-heterocyclic carbene ligands. a computational assessment, J. Organomet. Chem. 691 (2006) 4350–4358.

[77] S. G. Patra, N. K. Das, Recent advancement on the mechanism of olefin metathesis by grubbs catalysts: A computational perspective, Polyhedron 200 (2021) 115096–1–115096–25.

[78] E. Pump, A. Poater, N. Bahri-Laleh, R. Credendino, L. Serra, V. Scarano, L. Cavallo, Regio, stereo and chemoselectivity of 2nd generation grubbs ruthenium-catalyzed olefin metathesis, Catalysis Today (2020).

[79] J. A. M. Lummiss, F. A. Perras, R. McDonald, D. L. Bryce, D. E. Fogg, Sterically driven olefin metathesis: The impact of alkylidene substitution on catalyst activity, Organometallics 35 (2016) 691–698.

[80] K. Paredes-Gil, P. Jaque, Theoretical characterization of first and second generation grubbs catalysts in styrene cross–metathesis reactions: insights from conceptual DFT, Catal. Sci. Technol. 6 (2016) 755–766.

[81] C. Pietraszuk, H. Fischer, S. Rogalski, B. Marciniec, The effect of substituents at silicon on the cross-metathesis of trisubstituted vinylsilanes with olefins, J. Organomet. Chem. 690 (2005) 5912–5921.

[82] M. Brookhart, M. L. H. Green, G. Parkin, Agostic interactions in transition metal compounds, PNAS 104 (2007) 6908.

[83] X. Lin, W. Wu, Y. Mo, A theoretical perspective of the agostic effect in early transition metal compounds, Coord. Chem. Rev. 419 (2020) 213401–1–213401–18.

[84] E. Kraka, W. Zou, Y. Tao, M. Freindorf, Exploring the mechanism of catalysis with the unified reaction valley approach (urva) - a review, Catalysts 10 (2020) 691.

[85] Z. Konkoli, E. Kraka, D. Cremer, Unified Reaction Valley Approach Mechanism of the Reaction $CH_3 + H_2 \rightarrow CH_4 +$ H, J. Phys. Chem. A 101 (1997) 1742–1757.

[86] E. Kraka, Reaction Path Hamiltonian and the Unified Reaction Valley Approach, WIREs: Comput. Mol. Sci. 1 (2011) 531–556.

[87] E. Kraka, D. Cremer, Dieter cremer's contribution to the field of theoretical chemistry, Int. J. Quantum Chem. 119 (2019) e25849.

[88] E. Kraka, D. Cremer, Computational Analysis of the Mechanism of Chemical Reactions in Terms of Reaction Phases: Hidden Intermediates and Hidden Transition States, Acc. Chem. Res. 43 (2010) 591–601.

[89] D. Cremer, E. Kraka, From Molecular Vibrations to Bonding, Chemical Reactions, and Reaction Mechanism, Curr. Org. Chem. 14 (2010) 1524–1560.

[90] Y. Tao, W. Zou, S. Nanayakkara, E. Kraka, Pyvibms: A pymol plugin for visualizing vibrations in molecules and solids, J. Mol. Model. 26 (2020) 290–1–290–12.

[91] D. Cremer, A. Wu, E. Kraka, The Mechanism of the Reaction FH + $H_2C{=}CH_2 \rightarrow H_2C - CFH_3$. Investigation of Hidden Intermediates with the Unified Reaction Valley Approach, Phys. Chem. Chem. Phys. 3 (2001) 674–687.

[92] E. Kraka, D. Cremer, Mechanism and Dynamics of Organic Reactions: 1,2-H Shift in Methylchlorocarbene, J. Phys. Org. Chem. 15 (2002) 431–447.

[93] E. Kraka, A. Wu, D. Cremer, Mechanism of the Diels-Alder Reaction Studied with the United Reaction Valley Approach: Mechanistic Differences between Symmetry-Allowed and Symmetry-Forbidden Reactions, J. Phys. Chem. A 107 (2003) 9008–9021.

[94] H. Joo, E. Kraka, W. Quapp, D. Cremer, The Mechanism of a Barrierless Reaction: Hidden Transition State and Hidden Intermediates in the Reaction of Methylene with Ethene, Mol. Phys. 105 (2007) 2697–2717.

[95] E. Kraka, W. Zou, M. Freindorf, D. Cremer, Energetics and Mechanism of the Hydrogenation of XH$_n$ for Group IV to Group VII Elements X, J. Chem. Theory Comput. 8 (2012) 4931–4943.

[96] T. Sexton, E. Kraka, D. Cremer, Extraordinary Mechanism of the Diels-Alder Reaction: Investigation of Stereochemistry, Charge Transfer, Charge Polarization, and Biradicaloid Formation, J. Phys. Chem. A 120 (2016) 1097–1111.

[97] M. Freindorf, T. Sexton, E. Kraka, D. Cremer, The Mechanism of the Cycloaddition Reaction of 1,3-Dipole Molecules with Acetylene - An Investigation with the Unified Reaction Valley Approach, Theor. Chem. Acc. 133 (2013) 1423.

[98] T. M. Sexton, M. Freindorf, E. Kraka, D. Cremer, A Reaction Valley Investigation of the Cycloaddition of 1,3-Dipoles with the Dipolarophiles Ethene and Acetylene: Solution of a Mechanistic Puzzle, J. Phys. Chem. A 120 (2016) 8400–8418.

[99] C. S. López, O. N. Faza, M. Freindorf, E. Kraka, D. Cremer, Solving the Pericyclic-Pseudo pericyclic Puzzle in the Ring-Closure Reactions of 1,2,4,6-Heptatetraene Derivatives, J. Org. Chem. 81 (2015) 404–414.

[100] M. C. Reis, C. S. López, E. Kraka, D. Cremer, O. N. Faza, Rational Design in Catalysis: A Mechanistic Study of β-Hydride Eliminations in Gold(I) and Gold(III) Complexes Based on Features of the Reaction Valley, Inorg. Chem. 55 (2016) 8636–8645.

[101] M. Freindorf, D. Cremer, E. Kraka, Gold(I)-Assisted Catalysis - A Comprehensive View on the [3,3]-Sigmatropic Rearrangement of Allyl Acetate, Mol. Phys. 116 (2017) 611–630.

[102] S. Nanayakkara, M. Freindorf, Y. Tao, E. Kraka, Modeling hydrogen release from water with borane and alane catalysts: A unified reaction valley approach, J. Phys. Chem. A 124 (2020) 8978–8993.

[103] M. Freindorf, Y. Tao, D. Sethio, D. Cremer, E. Kraka, New Mechanistic Insights into the Claisen Rearrangement of Chorismate - A Unified Reaction Valley Approach Study, Mol. Phys. 117 (2018) 1172–1192.

[104] S. Nanayakkara, E. Kraka, A new way of studying chemical reactions: A hand-in-hand URVA and QTAIM approach, Phys. Chem. Chem. Phys. 21 (2019) 15007–15018.

[105] E. D. Glendening, C. R. Landis, F. Weinhold, NBO 6.0: Natural bond orbital analysis program, J. Comput. Chem. 34 (2013) 1429–1437.

[106] A. E. Reed, L. A. Curtiss, F. Weinhold, Intermolecular Interactions from a Natural Bond Orbital, Donor–Acceptor Viewpoint, Chem. Rev. 88 (1988) 899–926.

[107] C. R. Landis, F. Weinhold, The NBO View of Chemical Bonding, in: The Chemical Bond: Fundamental Aspects of Chemical Bonding, Wiley-VCH Verlag GmbH & Co. KGaA, 2014, pp. 91–120.

[108] F. Weinhold, C. R. Landis, E. D. Glendening, What is NBO Analysis and How is it Useful?, Int. Rev. Phys. Chem. 35 (2016) 39–440.

[109] E. Kraka, W. Zou, Y. Tao, Decoding chemical information from vibrational spectroscopy data: Local vibrational mode theory, WIREs: Comput. Mol. Sci. 10 (2020) 1480.

[110] Z. Konkoli, D. Cremer, A New Way of Analyzing Vibrational Spectra. I. Derivation of Adiabatic Internal Modes, Int. J. Quantum Chem. 67 (1998) 1–9.

[111] Z. Konkoli, J. A. Larsson, D. Cremer, A New Way of Analyzing Vibrational Spectra. II. Comparison of Internal Mode Frequencies, Int. J. Quantum Chem. 67 (1998) 11–27.

[112] Z. Konkoli, D. Cremer, A New Way of Analyzing Vibrational Spectra. III. Characterization of Normal Vibrational Modes in terms of Internal Vibrational Modes, Int. J. Quantum Chem. 67 (1998) 29–40.

[113] Z. Konkoli, J. A. Larsson, D. Cremer, A New Way of Analyzing Vibrational Spectra. IV. Application and Testing of Adiabatic Modes within the Concept of the Characterization of Normal Modes, Int. J. Quantum Chem. 67 (1998) 41–55.

[114] D. Cremer, J. A. Larsson, E. Kraka, New Developments in the Analysis of Vibrational Spectra on the Use of Adiabatic Internal Vibrational Modes, in: C. Parkanyi (Ed.), Theoretical and Computational Chemistry, Elsevier, Amsterdam, 1998, pp. 259–327.

[115] W. Zou, R. Kalescky, E. Kraka, D. Cremer, Relating Normal Vibrational Modes to Local Vibrational Modes with the Help of an Adiabatic Connection Scheme, J. Chem. Phys. 137 (2012) 084114.

[116] W. Zou, D. Cremer, C_2 in a Box: Determining its Intrinsic Bond Strength for the $X^1\Sigma^+_g$ Ground State, Chem. Eur. J. 22 (2016) 4087–4097.

[117] E. Kraka, J. A. Larsson, D. Cremer, Generalization of the Badger Rule Based on the Use of Adiabatic Vibrational Modes, in: J. Grunenberg (Ed.), Computational Spectroscopy, Wiley, New York, 2010, pp. 105–149.

[118] R. Kalescky, E. Kraka, D. Cremer, Identification of the Strongest Bonds in Chemistry, J. Phys. Chem. A 117 (2013) 8981–8995.

[119] E. Kraka, D. Cremer, Characterization of CF Bonds with Multiple-Bond Character: Bond Lengths, Stretching Force Constants, and Bond Dissociation Energies, ChemPhysChem 10 (2009) 686–698.

[120] E. Kraka, D. Setiawan, D. Cremer, Re-Evaluation of the Bond Length-Bond Strength Rule: The Stronger Bond Is not Always the Shorter Bond, J. Comp. Chem. 37 (2015) 130–142.

[121] D. Setiawan, D. Sethio, D. Cremer, E. Kraka, From Strong to Weak NF Bonds: On the Design of a New Class of Fluorinating Agents, Phys. Chem. Chem. Phys. 20 (2018) 23913–23927.

[122] D. Sethio, L. M. Lawson Daku, H. Hagemann, E. Kraka, Quantitative assessment of $B-B-B$, $B-H_b-B$, and $B-H_t$ bonds: From BH_3 to $B_{12}H_{12}^{2-}$, ChemPhysChem 20 (2019) 1967–1977.

[123] A. A. A. Delgado, A. Humason, R. Kalescky, M. Freindorf, E. Kraka, Exceptionally Long Covalent CC Bonds - A Local Vibrational Mode Study, Molecules (2021). In press.

[124] V. Oliveira, E. Kraka, D. Cremer, The Intrinsic Strength of the Halogen Bond: Electrostatic and Covalent Contributions Described by Coupled Cluster Theory, Phys. Chem. Chem. Phys. 18 (2016) 33031–33046.

[125] V. Oliveira, E. Kraka, D. Cremer, Quantitative Assessment of Halogen Bonding Utilizing Vibrational Spectroscopy, Inorg. Chem. 56 (2016) 488–502.

[126] V. Oliveira, D. Cremer, Transition from Metal-Ligand Bonding to Halogen Bonding Involving a Metal as Halogen Acceptor: A Study of Cu, Ag, Au, Pt, and Hg Complexes, Chem. Phys. Lett. 681 (2017) 56–63.

[127] S. Yannacone, V. Oliveira, N. Verma, E. Kraka, A continuum from halogen bonds to covalent bonds: Where do λ^3 iodanes fit?, Inorganics 7 (2019) 47.

[128] V. P. Oliveira, B. L. Marcial, F. B. C. Machado, E. Kraka, Metal-halogen bonding seen through the eyes of vibrational spectroscopy, Materials 13 (2020) 55.

[129] V. Oliveira, D. Cremer, E. Kraka, The Many Facets of Chalcogen Bonding: Described by Vibrational Spectroscopy, J. Phys. Chem. A 121 (2017) 6845–6862.

[130] V. Oliveira, E. Kraka, Systematic Coupled Cluster Study of Noncovalent Interactions Involving Halogens, Chalcogens, and Pnicogens, J. Phys. Chem. A 121 (2017) 9544–9556.

[131] D. Setiawan, E. Kraka, D. Cremer, Hidden Bond Anomalies: The Peculiar Case of the Fluorinated Amine Chalcogenides, J. Phys. Chem. A 119 (2015) 9541–9556.

[132] D. Setiawan, E. Kraka, D. Cremer, Strength of the Pnicogen Bond in Complexes Involving Group VA Elements N, P, and As, J. Phys. Chem. A 119 (2014) 1642–1656.

[133] D. Setiawan, E. Kraka, D. Cremer, Description of Pnicogen Bonding with the help of Vibrational Spectroscopy-The Missing Link Between

Theory and Experiment, Chem. Phys. Lett. 614 (2014) 136–142.

[134] D. Setiawan, D. Cremer, Super-Pnicogen Bonding in the Radical Anion of the Fluorophosphine Dimer, Chem. Phys. Lett. 662 (2016) 182–187.

[135] D. Sethio, V. Oliveira, E. Kraka, Quantitative Assessment of Tetrel Bonding Utilizing Vibrational Spectroscopy, Molecules 23 (2018) 2763–1–2763–21.

[136] M. Freindorf, E. Kraka, D. Cremer, A Comprehensive Analysis of Hydrogen Bond Interactions Based on Local Vibrational Modes, Int. J. Quantum Chem. 112 (2012) 3174–3187.

[137] R. Kalescky, W. Zou, E. Kraka, D. Cremer, Local Vibrational Modes of the Water Dimer - Comparison of Theory and Experiment, Chem. Phys. Lett. 554 (2012) 243–247.

[138] R. Kalescky, E. Kraka, D. Cremer, Local Vibrational Modes of the Formic Acid Dimer - The Strength of the Double H-Bond, Mol. Phys. 111 (2013) 1497–1510.

[139] Y. Tao, W. Zou, J. Jia, W. Li, D. Cremer, Different Ways of Hydrogen Bonding in Water - Why Does Warm Water Freeze Faster than Cold Water?, J. Chem. Theory Comput. 13 (2017) 55–76.

[140] Y. Tao, W. Zou, E. Kraka, Strengthening of Hydrogen Bonding With the Push-Pull Effect, Chem. Phys. Lett. 685 (2017) 251–258.

[141] M. Z. Makoś, M. Freindorf, D. Sethio, E. Kraka, New insights into Fe–H_2 and Fe–H^- bonding of a [nife] hydrogenase mimic – a local vibrational mode study, Theor. Chem. Acc. 138 (2019) 76.

[142] S. Lyu, N. Beiranvand, M. Freindorf, E. Kraka, Interplay of ring puckering and hydrogen bonding in deoxyribonucleosides, J. Phys. Chem. A 123 (2019) 7087–7103.

[143] R. F. W. Bader, A quantum theory of molecular structure and its applications, Chem. Rev. 91 (1991) 893–928.

[144] R. F. W. Bader, The quantum mechanical basis of conceptual chemistry, Monatshefte fŒr Chemie 136 (2005) 819–854.

[145] K. Fukui, The path of chemical reactions – the IRC approach, Acc. Chem. Res. 14 (1981) 363–368.

[146] H. P. Hratchian, E. Kraka, Improved Predictor-Corrector Integrators For Evaluating Reaction Path Curvature, J. Chem. Theory Comput. 9 (2013) 1481–1488.

[147] C. Lee, W. Yang, R. G. Parr, Development of the Colle–Salvetti correlation-energy formula into a functional of the electron density, Phys. Rev. B 37 (1988) 785–789.

[148] A. D. Becke, Density-functional thermochemistry. III. the role of exact exchange, J. Chem. Phys. 98 (1993) 5648–5652.

[149] R. Ditchfield, W. J. Hehre, J. A. Pople, Self-Consistent Molecular-Orbital Methods. IX. An Extended Gaussian-Type Basis for Molecular-Orbital Studies of Organic Molecules, J. Chem. Phys. 54 (1971) 724–728.

[150] D. Andrae, U. Häußermann, M. Dolg, H. Stoll, H. Preuß, Energy–adjusted ab initio pseudopotentials for the second and third row transition elements, Theoret. Chim. Acta 77 (1990) 123–141.

[151] M. J. Frisch, G. W. Trucks, H. B. Schlegel, G. E. Scuseria, M. A. Robb, J. R. Cheeseman, G. Scalmani, V. Barone, G. A. Petersson, H. Nakatsuji, X. Li, M. Caricato, A. V. Marenich, J. Bloino, B. G. Janesko, R. Gomperts, B. Mennucci, H. P. Hratchian, J. V. Ortiz, A. F. Izmaylov, J. L. Sonnenberg, D. Williams-Young, F. Ding, F. Lipparini, F. Egidi, J. Goings, B. Peng, A. Petrone, T. Henderson, D. Ranasinghe, V. G. Zakrzewski, J. Gao, N. Rega, G. Zheng, W. Liang, M. Hada, M. Ehara, K. Toyota, R. Fukuda, J. Hasegawa, M. Ishida, T. Nakajima, Y. Honda, O. Kitao, H. Nakai, T. Vreven, K. Throssell, J. A. Montgomery Jr, J. E. Peralta, F. Ogliaro, M. J. Bearpark, J. J. Heyd, E. N. Brothers, K. N. Kudin, V. N. Staroverov, T. A. Keith, R. Kobayashi, J. Normand, K. Raghavachari, A. P. Rendell, J. C. Burant, S. S. Iyengar, J. Tomasi, M. Cossi, J. M. Millam, M. Klene, C. Adamo, R. Cammi, J. W. Ochterski, R. L. Martin, K. Morokuma, O. Farkas, J. B. Foresman, D. J. Fox, Gaussian 16, Gaussian Inc. Wallingford CT, 2016.

[152] C. T. Campos, F. E. Jorge, Triple zeta quality basis sets for atoms Rb through Xe: application in CCSD(T) atomic and molecular property calculations, Mol. Phys. 111 (2013) 167–173.

[153] K. G. Dyall, Interfacing relativistic and nonrelativistic methods. I. normalized elimination of the small component in the modified Dirac equation, J. Chem. Phys. 106 (1997) 9618–9626.

[154] K. G. Dyall, A systematic sequence of relativistic approximations, J. Comput. Chem. 23 (2002) 786–793.

[155] M. Filatov, W. Zou, D. Cremer, Analytic Calculation of Isotropic Hyperfine Structure Constants Using the Normalized Elimination of the Small Component Formalism, J. Chem. Phys. A 116 (2012) 3481–3486.

[156] M. Filatov, W. Zou, D. Cremer, Analytic Calculation of Contact Densities and Mössbauer Isomer Shifts Using the Normalized Elimination of the Small-Component Formalism, J. Chem. Theory Comput. 8 (2012) 875–882.

[157] M. Filatov, W. Zou, D. Cremer, Relativistically Corrected Electric Field Gradients Calculated with the Normalized Elimination of the Small Component Formalism, J. Chem. Phys. 137 (2012) 054113.

[158] W. Zou, M. Filatov, D. Cremer, Analytic Calculation of Second-Order Electric Response Properties with the Normalized Elimination of the Small Component (NESC) Method, J. Chem. Phys. 137 (2012) 084108.

[159] M. Filatov, W. Zou, D. Cremer, On the Isotope Anomaly of Nuclear Quadrupole Coupling in Molecules, J. Chem. Phys. 137 (2012) 131102.

[160] T. Yoshizawa, W. Zou, D. Cremer, Calculations of Electric Dipole Moments and Static Dipole Polarizabilities Based on the Two-Component Normalized Elimination of the Small Component Method, J. Chem. Phys. 145 (2016) 184104.

[161] T. Yoshizawa, W. Zou, D. Cremer, Calculations of Atomic Magnetic Nuclear Shielding Constants Based on the Two-Component Normalized Elimination of the Small Component Method, J. Chem. Phys. 146 (2017) 134109.

[162] T. Yoshizawa, M. Filatov, D. Cremer, W. Zou, Calculation of contact densities and Mössbauer isomer shifts utilising the dirac-exact two-component normalised elimination of the small component (2c-NESC) method, Mol. Phys. 117 (2019) 1164–1171.

[163] W. Zou, M. Filatov, D. Cremer, Development and Application of the Analytical Energy Gradient for the Normalized Elimination of the Small Component Method, J. Chem. Phys. 134 (2011) 244117.

[164] W. Zou, M. Filatov, D. Cremer, Analytical Energy Gradient for the Two-Component Normalized Elimination of the Small Component Method, J. Chem. Phys. 142 (2015) 214106.

[165] W. Zou, M. Filatov, D. Cremer, Development, Implementation, and Application of an Analytic Second Derivative Formalism for the Nor-

malized Elimination of the Small Component Method, J. Chem. Theory Comput. 8 (2012) 2617–2629.

[166] D. G. Liakos, Y. Guo, F. Neese, Comprehensive benchmark results for the domain based local pair natural orbital coupled cluster method (DLPNO-CCSD(T)) for closed- and open-shell systems, J. Phys. Chem. A 124 (2020) 90–100.

[167] F. Weigend, R. Ahlrichs, Balanced basis sets of split valence, triple zeta valence and quadruple zeta valence quality for H to Rn: Design and assessment of accuracy, Phys. Chem. Chem. Phys. 7 (2005) 3297–3305.

[168] F. Neese, The ORCA program system, WIREs 2 (2012) 73–78.

[169] E. Kraka, W. Zou, M. Filatov, J. Gräfenstein, J. Gauss, Y. He, A. Wu, Z. Konkoli, Z. He, D. Cremer, et al., COLOGNE20, Computational and Theoretical Chemistry Group (CATCO), Southern Methodist University: Dallas, TX, USA, 2020.

[170] W. Zou, Y. Tao, M. Freindorf, M. Z. Makoś, N. Verma, E. Kraka, Local Vibrational Mode Analysis: LModeA, Computational and Theoretical Chemistry Group (CATCO), Southern Methodist University: Dallas, TX, USA, 2020.

[171] I. Mayer, Charge, bond brder an valence in the ab initio theory., Chem. Phys. Lett. 97 (1983) 270–274.

[172] I. Mayer, Bond orders and valences from ab initio wave functions., Int. J. Quantum Chem. 29 (1986) 477–483.

[173] I. Mayer, Bond order and valence indices: A personal account, J. Comput. Chem. 28 (2007) 204–221.

[174] T. A. Keith, AIMALL, 2017. TK Gristmill Software, Overland Park KS.

[175] D. Cremer, E. Kraka, Chemical Bonds without Bonding Electron Density? Does the Difference Electron-Density Analysis Suffice for a Description of the Chemical Bond?, Angew. Chem. Int. Ed. 23 (1984) 627–628.

[176] D. Cremer, E. Kraka, A description of the chemical bond in terms of local properties of electron density and energy, Croatica Chem. Acta 57 (1984) 1259–1281.

[177] E. Kraka, D. Cremer, Chemical Implication of Local Features of the Electron Density Distribution, in: Theoretical Models of Chemical Bonding. The Concept of the Chemical Bond, volume 2, Z.B. Maksic, ed., Springer Verlag, Heidelberg, 1990, pp. 453–542.

[178] N. Koga, S. Obara, K. Kitaura, K. Morokuma, Role of agostic interaction in β–elimination of palladium and nickel complexes. an ab initio MO study, J. Am. Chem. Soc. 107 (1985) 7109–7116.

[179] M. Palusiak, T. M. Krygowski, Application of AIM parameters at ring critical points for estimation of π–electron delocalization in six–membered aromatic and quasi–aromatic rings, Chem. Eur. J. 13 (2007) 7996–8006.